UNIVERSITY OF CALIFORNIA

Los Angeles

Tactile Sensors for Minimally Invasive Surgical Systems

A dissertation submitted in partial satisfaction of the

requirements for the degree Doctor of Philosophy

in Biomedical Engineering

by

Omeed Hamed Paydar

2016

© Copyright by

Omeed Hamed Paydar

2016

ABSTRACT OF THE DISSERTATION

Development of Capacitive Tactile Sensors for Minimally Invasive Surgical Systems

by

Omeed Hamed Paydar

Doctor of Philosophy in Electrical Engineering

University of California, Los Angeles, 2016

Professor Warren Grundfest, Co-Chair

Professor Robert N. Candler, Co-Chair

Minimally invasive surgery (MIS) improves patient outcomes. Operations result in smaller incisions, shorter recovery times, lower risk of infection, and reduced pain as compared to open surgery. Moreover, robotic surgical systems improve upon traditional laparoscopic tools used in MIS, including improved dexterity, tremor removal, scaled movements, and 3D visualization.

While the adoption of robotic surgical tools accelerates nationwide, these systems are characterized by an absence of touch sensation, which ultimately impedes transition of more delicate procedures. Likewise, excessive grip forces could induce tissue damage, including scar formation, hemorrhaging, perforations, and adhesions.

Furthermore, without tactile information, sutures fail because of excessive tensile loads and surgeons require additional training to reach proficiency on the available surgical robots.

Although robotics addresses a subset of surgical procedures, efforts to develop and integrate multi-axis biocompatible sensor arrays with commercial robotic surgical systems remain inadequate. New tools that measure compressive sensing could prevent tissue crush injuries, while shear sensing will help reduce suture failure from excessive tensile loads. Consequently, **this study investigates the development of a capacitive sensor capable of restoring touch sensation to surgeons operating robotic surgical systems.**

Real-time access to operative loads could minimize robotic surgical complications, and ultimately, lead to the inclusion of more challenging (demanding) procedures. This work explores a relatively under-researched, undeveloped area of robotic surgery and *the* major remaining challenge. Because minimally invasive surgery (MIS), specifically robotic surgery, is becoming more prevalent [1], efforts to improve the outcomes are essential. Successful acquisition of intraoperative tactile information will fast-track acceptance of these tools and prevent unwanted patient outcomes.

The dissertation of Omeed Hamed Paydar is approved.

Chang-Jin Kim

Pei-Yu Chiou

Warren Grundfest, Committee Co-Chair

Robert N. Candler, Committee Co-Chair

University of California, Los Angeles

2016

To my family. Thank you.

TABLE OF CONTENTS

Chapter 1 Introduction 1
1.1 History, Prevalence, and Predictions 1
1.2 Robotic Surgery 6
1.3 Benefits of Minimally Invasive Surgery 8
1.4 Significance of Tactile Information 10
1.5 Prior Art (maybe move to design chapter, before our design) 12
Chapter 2 Design 15
2.1 Sensor Location 15
2.2 Performance Criteria 18
2.2.1 Sizing 18
2.2.2 Sensitivity and Dynamic Range 19
2.2.3 Temporal Resolution 21
2.3 Working Principle 22
2.3.1 Parallel Plate Capacitive Sensor 22
2.3.2 Combined Compressive and Shear Sensor 22
2.4 Theory 27
2.4.1 Parallel Plate Capacitor 27
2.4.2 Combined Compressive and Shear Sensor 28
Chapter 3 Fabrication 36
3.1 Microfabrication 36
3.1.1 Parallel Plate Capacitor 37
3.1.2 Combined Compressive and Shear Sensor 39
3.2 Printed Circuit Board (PCB) Fabrication 44
3.2.1 Parallel Plate PCB 44
3.2.2 Combined Sensor PCB 45
Chapter 4 Results 48
4.1 Parallel Plate Capacitor 48
4.2 Combined Compressive and Shear Sensor 53
4.3 Summary and Conclusion 58

LIST OF FIGURES

Figure 1. Growth rates for laparoscopic surgery. Blue bars represent 5-year growth and red bars represent 10-year growth. The decrease for tubal ligation can be attributed to non-surgical approaches that have proven effective. Data were acquired in 2011. [10] 4
Figure 2. National minimally invasive surgery volume by type of procedure (left axis) and aggregate (right axis). The semi-transparent blue bar represents the sum of the individual procedures and highlights the total number of procedures (in millions) performed minimally invasively in 2011 and forecasting for 2016 and 2021. The colored bars represent the breakdown of the total number by surgical procedure (in thousands) [10]]. The 2.9 million procedures in 2011 make up nearly 6% of the total procedures performed nationally. 5
Figure 3. Robotic surgery prevalence. Data presented represents the number of robotic surgical cases for successive years from 2004-2011. The black bars represent domestic data while the gray bars represent international data. [13] 7
Figure 4. Typical incision patterns for laparoscopic and open surgical procedures. A laparoscopic (left) approach is characterized by multiple small incisions and reduced trauma to the patient. Traditional open (right) surgical approaches result in larger incisions to gain access to the underlying tissue, an approach that requires longer hospital stays and prone to more complications. 9
Figure 5. Plots representing the duration of applied load and the magnitude of the grasping force for four population groups during a phantom surgical task. Participants were asked to dissect a synthetic artery from synthetic tissue in five minutes. The magnitude of the applied force during this surgical task was elevated in the absence of force feedback (FF). Increasing the feedback gain resulted in lighter and longer application of force. Adapted from [19]]. 11
Figure 6. Plots representing the root mean square of force, peak force, number of errors, and length dissected for each population group as a function of the force feedback gain. For each metric, the addition of force feedback resulted in improvements in the surgical task. The length dissected plot represents a performance metric demonstrating that the addition of force feedback did not result in slower dissections. 11
Figure 7. Surgical sensor system prior art. Here the red outline represents sensors located at the grasper handle; green represents a sensor solution in the grasper shaft; and blue represents sensor solutions integrated at the grasper tip. Research groups have proposed different sensing modalities, including optical sensing, capacitive sensing, and force estimation based on servo output. 14

Figure 8. Locations on the robotic grasper that have been identified as possible locations for sensor systems. Each region is characterized by advantages and disadvantages. Different research groups have implemented sensor solutions in every region. Beige arc in the center of the figure represents the abdominal cavity where regions to the left are outside the body and those to the right are inside the body. [26]..... 15
Figure 9. Mechanoreceptors on the finger pads. Each receptive field feeds back information from mechanical stimuli to the corresponding receptor. The size of the receptive field dictates the size of the sensor elements. Too large, and the sensor will trigger multiple receptive fields. Too small and tactile information will disappear at the tactile display. Adapted from M. J. Malachowski's schematic.. 19
Figure 10. The finger detection limits and the upper bound typical of laparoscopic surgery. The sensor must be capable of responding over the entire dynamic range (1 mN to 20 N) with adequate sensitivity to capture the tissue-grasper interaction over the course of a procedure.. 21
Figure 11. Cartoon representation of temporal resolution of tactile feedback system. The real-time visual feedback (hare to the cartoon eyes) must not precede the tactile feedback (tortoise to the fingertips) by more than 330 milliseconds. Delays exceeding this threshold result in distractions that impede instead of aid surgery. 21
Figure 12. Schematic representation of the combined normal and shear sensor. The top plate, dielectric, and bottom plate are represented in top-view (top half) and cross section (bottom half) through the AA' line. The top metal plate consisted of 7 separate electrodes, two of which (C_{comp}) were required for compressive sensing and the remaining created the shear sensor. 23
Figure 13. Combined sensor working principle in response to compressive load. When a compressive load was applied to the top plate of the capacitor, the gap between the top plate and bottom plate decreased resulting in an increase in the capacitance. The measured capacitance was the series combination of the two C_{comp} components through the bottom plate. Because the shear sensing is a differential measurement, no change is detected through the shear sensor elements. 24
Figure 14. Combined sensor working principle in response to shear load in the positive x (from left to right) direction. A shear load causes a change in the overlap area. In the case of a shear load in the positive x direction, the elements translate to the right, which cause an increase in the overlap of the left element and a similar decrease in the overlap of the right element. This causes an increase in capacitance on the left and a decrease on the right and no change to the excitation capacitance (C_{exc}). The resulting shear load could be quantified by looking at the

differential measurement, or change, due to the change in the overlap area. The same principle could be applied if the shear vector were in the y direction (top to bottom) or if the shear were applied at any arbitrary angle. 26
Figure 15. Calculation of the *compressive* output response of different second-generation capacitor designs in response to applied load. The main take away is the sensitivity (slope) increases with larger capacitive plates and by decreasing the initial gap between the top and bottom electrodes. The solid lines represent the analytical solution without simplifying assumptions, while the dashed lines represent the linear approximation..... 33
Figure 16. Calculation of the shear output response of different second-generation capacitor dielectric thicknesses in response to an applied shear load. The main take away is the sensitivity (slope) increases with a decreasing dielectric gap. Because the shear capacitance measurement is a differential measurement, in the absence of an applied load, the expected output would be 0 F. Shear in one direction would result in a positive differential capacitance and shear in the opposite direction would result in a negative differential shear..... 35
Figure 17. Two generations of capacitive sensors. (left) The single sensor element is capable of detecting typical surgical compressive loads. Compression results in a smaller gap between the top and bottom plates and therefore an increase in capacitance, which could then be used to determine the magnitude of the deflected load. (right) The combined compression and shear sensor. The compression can be sensed with a change in the dielectric thickness, while a change in the overlap area of the perimeter electrodes allow for detection and quantification of shear loads. 36
Figure 18. Fabrication steps for the parallel plate capacitive sensor. (1) Fabrication began with a single 4-inch glass wafer. (2) The bottom electrode was formed by an electron-beam-evaporated metal layer and lift-off of a previously developed photoresist. (3) The dielectric layer was formed by a chemical vapor deposition (CVD) of a 1-micron layer of Parylene C. (4) Vias were selectively etched into the dielectric with a reactive ion etch (RIE) process to create access to the underlying metal layer. (5) A second evaporation step and lift-off defined the top metal electrode. (6) The integration with the read-out circuit was accomplished with wire bonding to the sensor bond pads. 38
Figure 19. Final first-generation fabricated sensor array. A representative 3x2 array of 1-mm^2 sensors is presented. Dark edges outline areas where the Parylene C have been selectively etched away, including areas over the bond pads and lanes between adjacent sensor arrays. 39

Figure 20. Sensor fabrication steps of the combined compression and shear sensor. (1) The fabrication began with an oxidized substrate to isolate the single. (2) The bottom metal plate was photolithographically defined and realized by liftoff of an evaporated titanium and gold layer. (3) Cleaving lines were etched into the backside of the wafer to simplify isolation of the individual sensors after fabrication was completed. (4) The wafers were then spin-coated with a thin polydimethylsiloxane (PDMS) layer to separate the top and bottom metal plates. (5) The top metal elements were also photolithographically defined and lifted off to reveal the final gold electrodes. (6) The samples were cleaved and isolated for testing and ultimately for integration with the grasper. 41
Figure 21. Interferometer measurement of metal on PDMS. (left) The profile shows the metal was successfully deposited on the PDMS surface without cracking and the average surface roughness is ~1 micron. (right) The profile shows the bare PDMS surface with average surface roughness of ~0.5 micron as a comparison. 42
Figure 22. Ridges and grooves of PDMS substrate with a thin evaporated metal blanket. 43
Figure 23.. Schematic of the capacitive sensing circuit. The circuit is composed of a Schmitt trigger buffer, inverter, buffer, two switches, resistor and the sensing capacitor (C_{DUT}). 44
Figure 24. Equivalent circuits for phase 1 and phase 2. 45
Figure 25. Schematic of printed circuit board design layout. The 2 layer board allowed for multiple connections to the 7-electrode configuration of the combined compression and shear sensor. The board was designed to integrate with the analog sensor output on one end and digitized by separate capacitance to digital chips for shear and compression sensing. 46
Figure 26. Populated printed circuit board. The final sensor was integrated with the board with the backside of the substrate exposed. This allowed for the protection of the delicate front side of the sensor, distribution of the load over the entire sensor surface, and simple one-sided integration with the PCB. 47
Figure 27. Schematic illustration of testing setup for wafer-level sensor characterization. An Agilent 4294A precision impedance analyzer in a four-point testing configuration is used to simultaneous stimulate and measure the performance of the capacitive sensor over a range of frequencies. 48
Figure 28. Measured baseline capacitance. The mean and standard deviation (dashed lines) of six capacitive sensors from a single capacitive array are plotted as a function of the measurement frequency. The frequency-dependent behavior of the sensor is due to the non-

constant dielectric constant of the Parylene C dielectric material. The measured capacitance exhibits a 2.5% error from theoretically predicted values. 49
Figure 29. Wafer-level compression testing setup. (Left) A 4-axis micromanipulator applies a vertical load to the capacitive sensor. The capacitance is measured through the probes and the adjacent impedance analyzer. (right) A close up of the force applicator and the load cell. 50
Figure 30. Capacitive response to an applied load. The sensor was subjected to progressive loads and the output capacitance was plotted for each applied load. A solid line represents the linear fit of the response, the slope of which corroborates with the calculated capacitive sensitivity. The expectation is that compressive loads decrease the size of the gap between the top and bottom plate, resulting in an increase in the capacitance. 51
Figure 31. Output of a Schmitt trigger switching circuit. The frequency of the output is inversely proportional to the capacitance and more specifically to the inverse of the time constant. Essentially, as the capacitance increases the frequency of the switching circuit decreases..... 52
Figure 32. Histogram of the number of counts of frequency from the output of the switching circuit. The switching circuit was fed into a frequency counter where the baseline frequency was 3.02 MHz. A one-newton load was applied to the capacitive sensor and the frequency of the circuit shifted downward. The response was measured to be 2 kHz/N. 53
Figure 33. The test setup for compression sensing. Forces were applied by an Instron universal testing machine onto the sensor surface. The capacitance to digital chip gave a direct digital output from the sensor, which was captured by the sensor software. The same PC powered the capacitance to digital converter chip (CDC), while a separate PC controlled the application of force. 54
Figure 34. The sensor output in response to a compressive load. The theoretical sensor output, in terms of relative change to the baseline value, is presented by a red trace. The data points are the measured output as a function of the applied load in Newtons. 55
Figure 35. The shear response of the combined sensor. The blue and pink semi-transparent bars on the plot represent shear in the positive and negative x direction, respectively. Shear in the positive x direction resulted in a negative differential capacitance, while shear in the negative x direction resulted in a positive differential measurement. Positive and negative peaks represent a static load condition in either direction. Release of the applied load resulted in a return to baseline. The initial offset from zero resulted from alignment error during the fabrication process where the area of the sensor elements over the bottom electrode plate was not identical. 56

Figure 36. Derivative of the shear sensor output from the data in figure 34. Real-time calculations of the derivative of the shear plot could give indications of slipping events. 58

LIST OF TABLES

Table 1. Overview of MIS adoption rates and future forecasts. 3
Table 2. Comparison Between Minimally Invasive Surgery and Traditional Open Surgery 9
Table 3. Tip-integrated sensor technologies 17

ACKNOWLEDGMENTS

This work was only possible because of the support of many friends, family members, and colleagues.

I'm forever grateful to Professor Robert Candler for his unwavering support. After my first advisor abandoned his students to pursue personal interests, Prof. Candler immediately offered an opportunity to join his research group. He allowed us to pursue our passions; he encouraged us to work hard; and always supported our individual direction.

To the members of the committee: Dr. Grundfest, Dr. Dutson, Dr. Kim, and Dr. Chiou, thank you for your guidance, for shaping the project, for supporting the work, and for infinite advice and encouragement.

My colleagues created a wonderful environment to share ideas and we grew together. Yongha Hwang, it's impossible to express my gratitude; thank you for everything! To all the members of the Candler team: Hyunmin Sohn, Jere Harrison, Srikanth Iyer, Jonathan Lake, Jimmy Wu, Sidhant Tiwari, Yuan Dai, Ling Li – thank you. I'm also thankful for the mentorship from members of my previous lab; their influence at the beginning of my graduate career was invaluable.

To my friends, thank you for your support and for making this Ph.D. process so enjoyable. I'm very appreciative for the support when things were challenging and I was fortunate to make some life-long friendships at UCLA.

To my brother, Naveed, I love you. Congratulations as you also complete your Ph.D – I'm very proud of you. To Bogie, I can't wait for fishing and fetch with you soon.

I owe everything to my family. I'm fortunate to have the most supportive parents. My goal was and always is to make you happy and proud. I love you both. To my grandparents and my extended family, I'm thankful for everything.

Lastly, to Gabi I cherish your support, your friendship, your excitement, and your drive. You motivate me, you encourage me, you challenge me, and you make me smile. I love you.

VITA

2008	B.S. Biomedical Engineering Purdue University West Lafayette, IN
2015	Alcon Laboratories

PUBLICATIONS

Journal publications

[1] **Omeed H. Paydar***, Yongha Hwang*, and Robert N. Candler. *Pneumatic microfinger with balloon fins for linear motion using 3D printed molds*. Sensors and Actuators A: Physical. Volume 234, 65-71, October 2015

[2] **Omeed H. Paydar***, Yongha Hwang*, and Robert N. Candler. *3D printed molds for non-planar PDMS microfluidic channels*. Sensors and Actuators A: Physical. Volume 226, 137-142, May 2015

[3] **Omeed H. Paydar***, Yongha Hwang*, Max Ho, James B. Rosenzweig, and Robert N. Candler. *Electrochemical macroporous silicon etching with current compensation*. Electronics Letters, 50 (19), 1373-1375, 2014

[4] Jere Harrison, Abhijeet Joshi, Yongha Hwang, **Omeed H. Paydar**, Jonathan Lake, Pietro Musumeci, and Robert N. Candler. *Surface-micromachined Electromagnets for 100 μm-scale Undulators and Focusing Optics*. Physics Procedia, 52, 19-26, 2014

[5] Jere Harrison, **Omeed H. Paydar**, Yongha Hwang, Jimmy Wu, Evan Threlkeld, Pietro Musumeci, and Robert N. Candler. *Fabrication Process For Thick-Film Micromachined Multi-Pole Electromagnets*. JMEMS IEEE/ASME Journal of Microelectromechanical Systems, 23 (3), 505-507, 2014

[6] **Omeed H. Paydar**, Carlo N. Paredes, Yongha Hwang, Joseph Paz, Neal B. Shah, and Robert N. Candler. *Characterization of 3D-Printed Microfluidic Chip Interconnects with Integrated O-Rings.* Sensors and Actuators A, 205, 199-203, 2014

Conference publications

[1] **Omeed H. Paydar***, Ahmad, Abiri*, Erik Dutson, Bradley Genovese, Usah Khrucharoen, and Warren Grundfest. *Suture Strength for Robotic Surgery.* Society of American Gastrointestinal and Endoscopic Surgeons (SAGES), 2015

[2] Aram J. Chung, C. -Y. Wu, Derek E. Go, J.C. Oka, **Omeed H. Paydar**, Robert N. Candler, Dino Di Carlo. *Complex 3D Shaped Particle Fabrication Via Inertial Flow Deformation and UV Polymerization*. The 17th International Conference on Miniaturized Systems for Chemistry and Life Sciences, 2013

[3] Jere Harrison, Abhijeet Joshi, Yongha Hwang, **Omeed H. Paydar**, Jonathan Lake, Pietro Musumeci, and Robert N. Candler. *Surface-Micromachined Electromagnets for 100 μM-Scale Undulators and Focusing Optics*. Physics Procedia, Workshop on Physics and Applications of High Brightness Beams, 2013

[4] **Omeed H. Paydar**, Christopher R. Wottawa, Richard E. Fan, Erik P. Dutson, Warren S. Grundfest, Martin O. Culjat, and Robert N. Candler. *Fabrication of a Thin-Film Capacitive Force Sensor Array for Tactile Feedback In Robotic Surgery*. IEEE Engineering in Medicine and Biology Conference (EMBC), 2012

Chapter 1 Introduction

Minimally invasive surgery (MIS) improves patient outcomes. Generally, minimally invasive surgery (also known as *laparoscopic surgery*) defines a broad range of procedures characterized by small incisions, shorter recovery time, and reduced patient trauma. Yet, this technique is only applicable to qualified candidates and a subset of the total surgical procedures.

While MIS offers several advantages to the patient, it introduces new surgical challenges. Surgeons require additional training beyond general surgery requirements and proficiency requires an increased number of surgical cases. Once trained, MIS procedures on average take longer than identical open procedures, which can lead to additional patient complications. Although *robotic* minimally invasive surgery (section 1.2) introduces additional benefits, including improved dexterity and greater precision, this technique does little to restore the lost tactile information. The absence of tactile information is introduced by the laparoscopic tools, which prevent direct contact between the internal tissues and the physician hand and without touch sensation, the patient can experience complications from excessive forces.

1.1 History, Prevalence, and Predictions

In 1901, German-born internist Georg Kelling pioneered the first laparoscopic examination on a canine. Although, he had referred to this procedure as “coelioscopy”, the process involved creation of a small incision in the abdominal wall and insertion of a trocar for insufflation prior to examination with a cystoscope. Borrowing from these techniques, Hans Christian Jacobaeus, a Swedish internist, first reported the

laparoscopic surgical approach in humans in 1910 [2, 3]. Although primarily for diagnostic purposes, Jacobaeus recognized the implications of laparoscopy and dedicated efforts to improving the laparoscopic instruments and understanding the challenges and limitations of this approach.

Over the next several decades, improvements to the techniques and instruments increased the popularity of laparoscopy. The progression of optics, including real-time magnification of the abdominal (*laparoscopic*) and thoracic (*thoracoscopic*) cavities and projection onto a television monitor created an opportunity to perform more complicated procedures [4]. These developments enabled Brazilian Tarasconi to perform and publish the first organ (fallopian tubes) resection in 1981 [5]. In the prior year, Semm [6] completed the first endoscopic appendectomy and published the results in 1983 [7].

In 1985, German physician Erich Mühe, in collaboration with Hans Frost developed the “Galloscope”, and performed an early version of a laparoscopic cholecystectomy (LC), or the surgical removal of the gallbladder [8]. The improvement in patient outcomes from LC, specifically shorter recovery times, attracted patients (and surgeons) to minimally invasive surgery. Today, minimally invasive surgery constitutes nearly six percent of the 51 million procedures nationally [9], including 1 million laparoscopic cholecystectomies.

Minimally invasive surgery is becoming more ubiquitous and, in fact, has become the standard of care for several procedures. Table 1 [10] summarizes the adoption rates of select core procedures, including forecasts to 2021. The rightmost column represents the percentage of cases that are completed laparoscopically (*i.e.,* 75% of all appendectomy surgeries were laparoscopic, as compared to 25% through traditional

open surgical procedures). The data suggest an increase in minimally invasive surgery prevalence in the forthcoming decade, and financial implications (*e.g.,* $50 Billion annually by 2019) [11] which would require rethinking hospital strategies.

Table 1. Overview of MIS adoption rates and future forecasts.

Procedure	National volume forecast (Thousands)			National volume growth rates (%)		MIS adoption (%)
	2011	2016	2021	5-year	10-year	
Appendectomy	359	363	391	1	9	75
Cholecystectomy	1006	1160	1300	9	22	96
Colectomy	369	431	505	17	37	8-15
Gastric bypass	63	68	75	8	20	80-90
Hysterectomy	641	647	646	1	1	40
Myomectomy	43	46	N/A	7	N/A	87
Prostatectomy	93	100	105	8	13	85
Tubal ligation	211	201	201	-5	-5	93
Ventral hernia repair	105	104	106	-1	0	25

Reprinted from [10]

The number and type of procedures have escalated due to improvements to the technology, patient and surgeon familiarity, and advances in surgeon skill. Table 1 shows some of the most common laparoscopic procedures and the percentage of cases performed minimally invasively. The adoption percentage is influenced by the existence of alternate approaches, access to laparoscopic tools and equipment, and difficulty of the operation.

Moreover, the number of surgical cases continues to grow. Figure 1 highlights the increase in the number of surgeries (in percent), for 5-year and 10-year time frames. The projections show that for the majority of common surgeries already performed laparoscopically, the number will grow in the coming years.

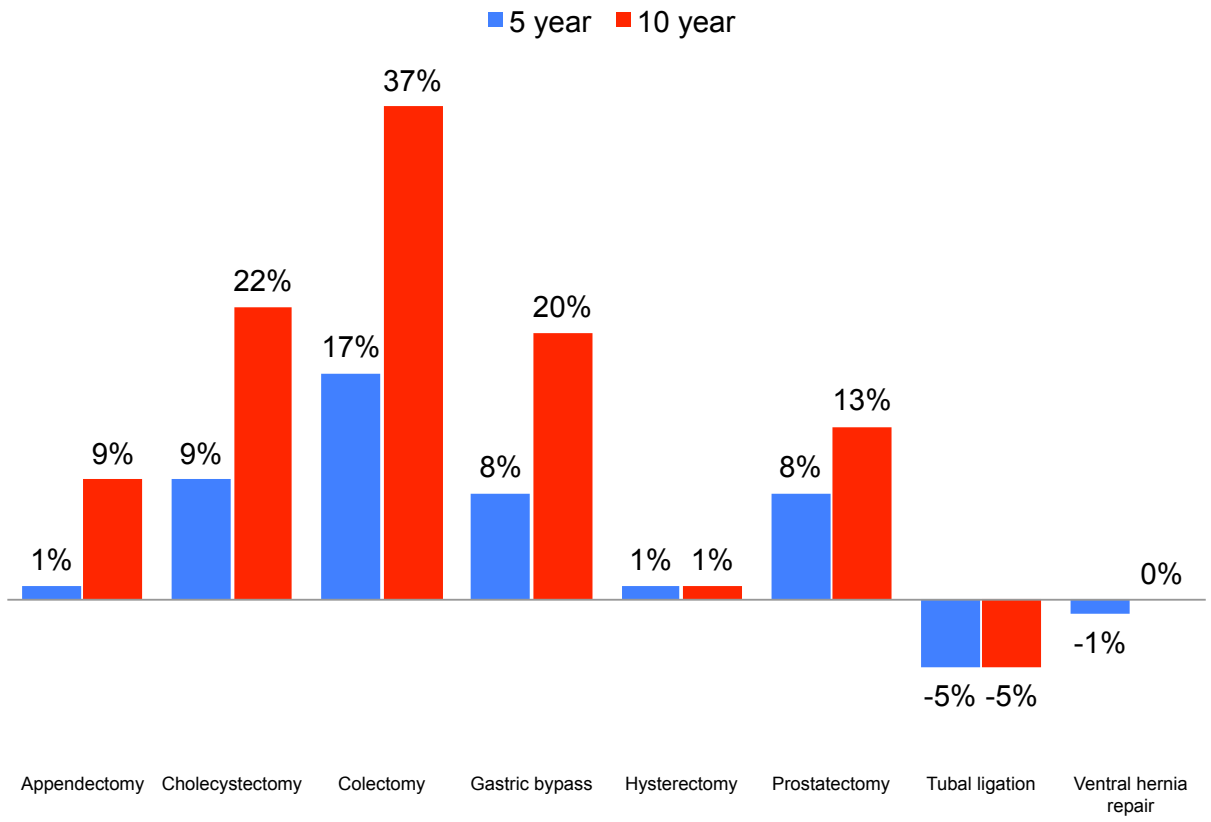

Figure 1. Growth rates for laparoscopic surgery. Blue bars represent 5-year growth and red bars represent 10-year growth. The decrease for tubal ligation can be attributed to non-surgical approaches that have proven effective. Data were acquired in 2011. [10]

In fact, of the eight procedures listed, only one of them, tubal ligation, is projected to see a reduction in both the five- and 10-year time frames. The reason for this reduction is not due to any deficiencies of the surgical approach, but because of less-invasive non-surgical options that result in similar outcomes for the patient.

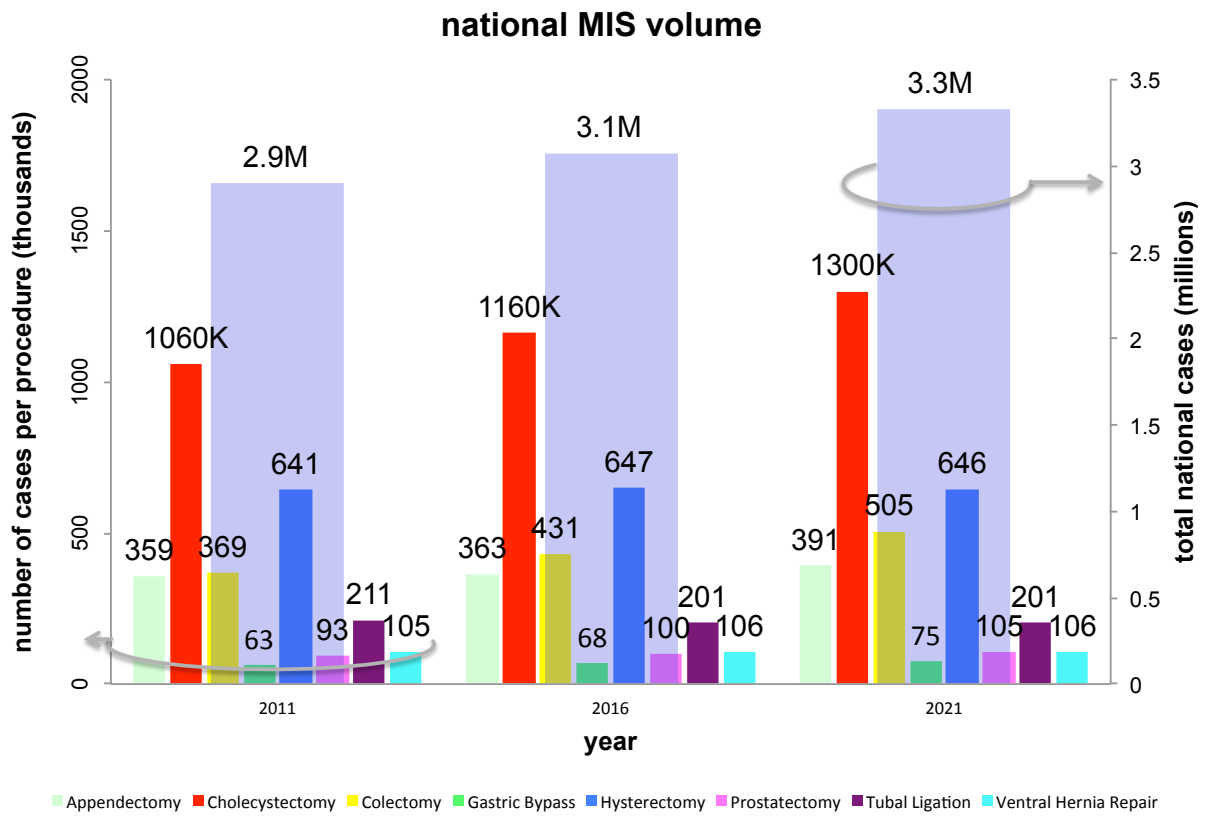

Figure 2. National minimally invasive surgery volume by type of procedure (left axis) and aggregate (right axis). The semi-transparent blue bar represents the sum of the individual procedures and highlights the total number of procedures (in millions) performed minimally invasively in 2011 and forecasting for 2016 and 2021. The colored bars represent the breakdown of the total number by surgical procedure (in thousands) [10]]. The 2.9 million procedures in 2011 make up nearly 6% of the total procedures performed nationally.

However, even with the growth-rate data, the argument still has to be made that the current market for minimally invasive surgery necessitates advances in technology. Specifically, the surgical volume must be large enough for investments to be made to improve the current technology and modify existing equipment. If the available technology is adequate and the number of patients benefiting from these tools is minimal, one could effectively argue that additional resources are not required into this less-than-effective approach. To that end, a 2011 assessment of the number of surgical

cases demonstrate that total number of surgical cases nationwide amounted to 2.9 million. This figure makes nearly 6% of the total 50+ million surgical cases according to the Centers of Disease Control (CDC) [12]]. This data, along with the 5- and 10-year projections, suggest that minimally invasive techniques have and will continue to be a viable healthcare option and a significant part of the future of healthcare.

1.2 Robotic Surgery

It is envisioned that robotics will play an ever-increasing role. These instruments will undoubtedly create new surgical options for more delicate surgical procedures and continue to improve upon the laparoscopic standard of care.

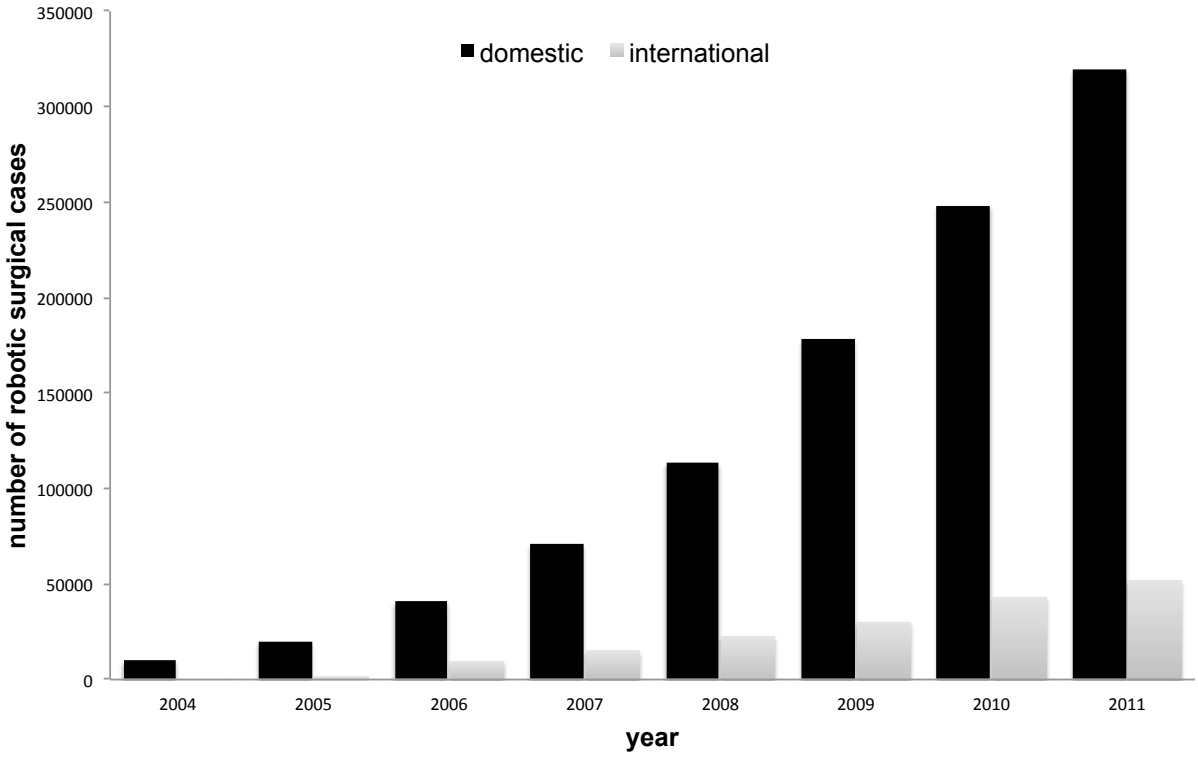

Figure 3. Robotic surgery prevalence. Data presented represents the number of robotic surgical cases for successive years from 2004-2011. The black bars represent domestic data while the gray bars represent international data. [13]

The data in Figure 3 shows the number of robotic surgical cases both domestically and internationally from 2004 to 2011. While the number of cases grows by an order of magnitude in the 7-year span, the number of robotic cases makes up only 10% of the total nationwide cases in 2011. If hospitals continue to adopt (and can afford) these robotic surgical suites, the percentage of surgeries performed robotically will continue to increase. Logically, an increase in the number of robotic cases will result in increased proficiency, and by proxy an increase in new use cases for robotics. Both of these results will accelerate adoption of surgical robots and the number of robotic cases.

The commercially available robotic surgical systems of today are lacking tactile feedback and evidence suggests that a lack of feedback can lead to excessive grip forces, tissue crush injuries, and ruptured sutures [14].

Delicate laparoscopic procedures require robotic surgical systems. These systems offer advantages over traditional laparoscopic surgery, including three additional degrees of motion, tremor removal, and elimination of the *fulcrum effect*-- the consequence of manipulating internal tissues and organs with laparoscopic instruments outside the body.

Surgical robots first appeared in 1985, when Kwoh et al. leveraged an industrial *programmable universal manipulation arm* (PUMA 560) for a neurobiopsy application. [15] Indisputably, robotic surgery platforms provide the same benefits as traditional minimally invasive surgery, including smaller incisions, shorter recovery times, lower risk of infection, and reduced pain as compared to open surgery. Moreover, robotic

surgical systems improve upon traditional laparoscopic tools, including improved dexterity, tremor removal, scaled movements, and 3D visualization [16].

While the adoption of robotic surgical tools accelerates nationwide [1], these systems are characterized by an absence of touch sensation, which ultimately impedes transition of more delicate procedures. Likewise, excessive grip forces could induce tissue damage, including scar formation, hemorrhaging, perforations, and adhesions [17]. Furthermore, without tactile information, surgeons require additional training to reach proficiency on the available surgical robots [18].

Although robotics addresses a subset of surgical procedures, efforts to develop and integrate biocompatible sensor arrays with commercial robotic surgical systems remain inadequate. Consequently, this study investigates sensing technologies capable of restoring touch sensation.

1.3 Benefits of Minimally Invasive Surgery

Both robotic and traditional laparoscopic surgery, have several advantages over conventional open surgery, where the surgeon often makes a single large incision to gain access to the abdominal cavity. During an MIS operation, the surgeon makes multiple smaller incisions (Figure 4) for insertion of the surgical instruments and optics to perform the procedure. Consequently, the patient experiences less pain and fewer traumas, which result in shorter hospital stays, fewer complications and cost savings. A more-complete comparison between MIS and conventional open surgery is presented in Table 2.

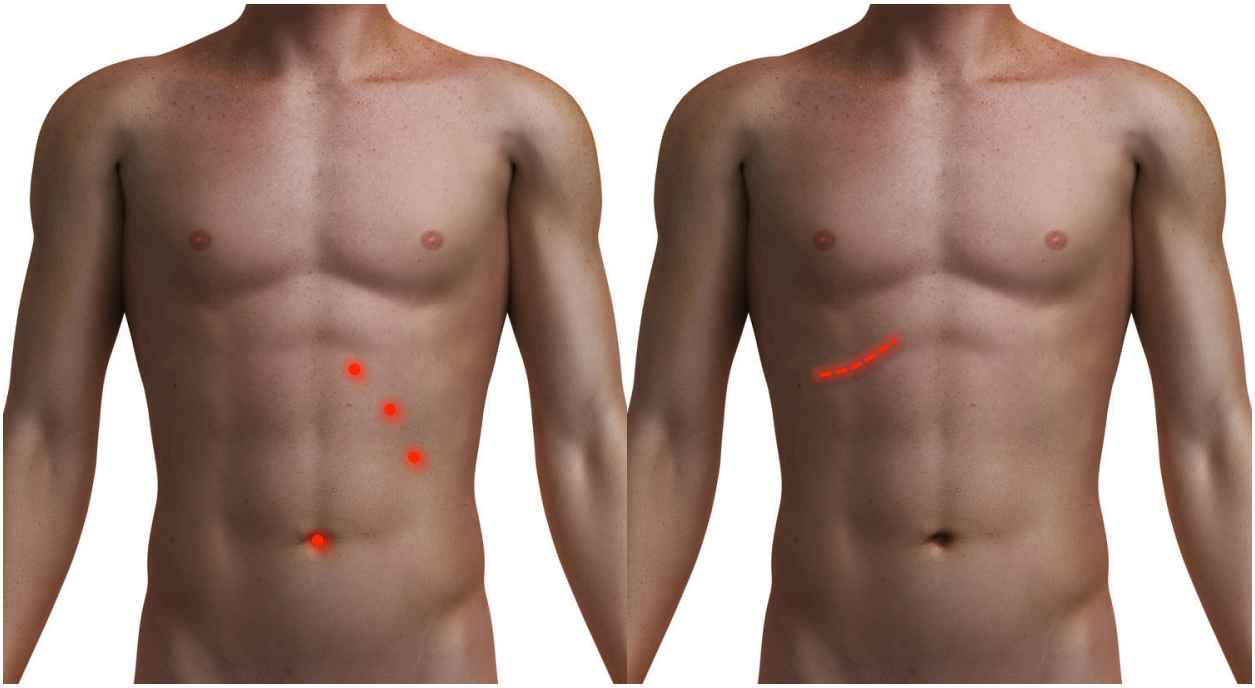

Figure 4. Typical incision patterns for laparoscopic and open surgical procedures. A laparoscopic (left) approach is characterized by multiple small incisions and reduced trauma to the patient. Traditional open (right) surgical approaches result in larger incisions to gain access to the underlying tissue, an approach that requires longer hospital stays and prone to more complications.

Robotic and traditional minimally invasive surgeries both offer several advantages to the patient at the expense of the surgeon. The major disadvantage of all MIS, however, is the lack of tactile feedback.

Table 2. Comparison Between Minimally Invasive Surgery and Traditional Open Surgery

	Laparoscopic (MIS)	**Robotic MIS**	**Open**
Advantages	• Minimal scarring • Reduced trauma • Shorter recovery time	• All benefits of MIS • Tremor removal • 3D vision • Scaled movements	• Direct patient contact • Surgeon familiarity • Availability
Disadvantages	• Diminished tactile feedback • No 3D vision • Poor dexterity	• Absence of tactile feedback • Longer surgeries • Expensive tooling	• Long recovery periods • Scar formation • Painful

1.4Significance of Tactile Information

The significance of tactile information can be explained by illustrating the effects of its absence. Wagner et al. [19] tasked medical students, surgical residents, senior surgical residents, and attending surgeons to dissect a 10-centimeter-long synthetic artery from synthetic tissue. The model materials were designed and chosen to simulate the actual mechanical properties of real tissues. The participants were quantitatively assessed on their ability to perform the dissection quickly and accurately while minimizing errors. The magnitude and duration of the applied loads during this surgical task (Figure 5) were elevated in the absence of force feedback (FF). Increasing the feedback gain resulted in lighter and longer application of force, which could result in a lower risk of injury during surgery.

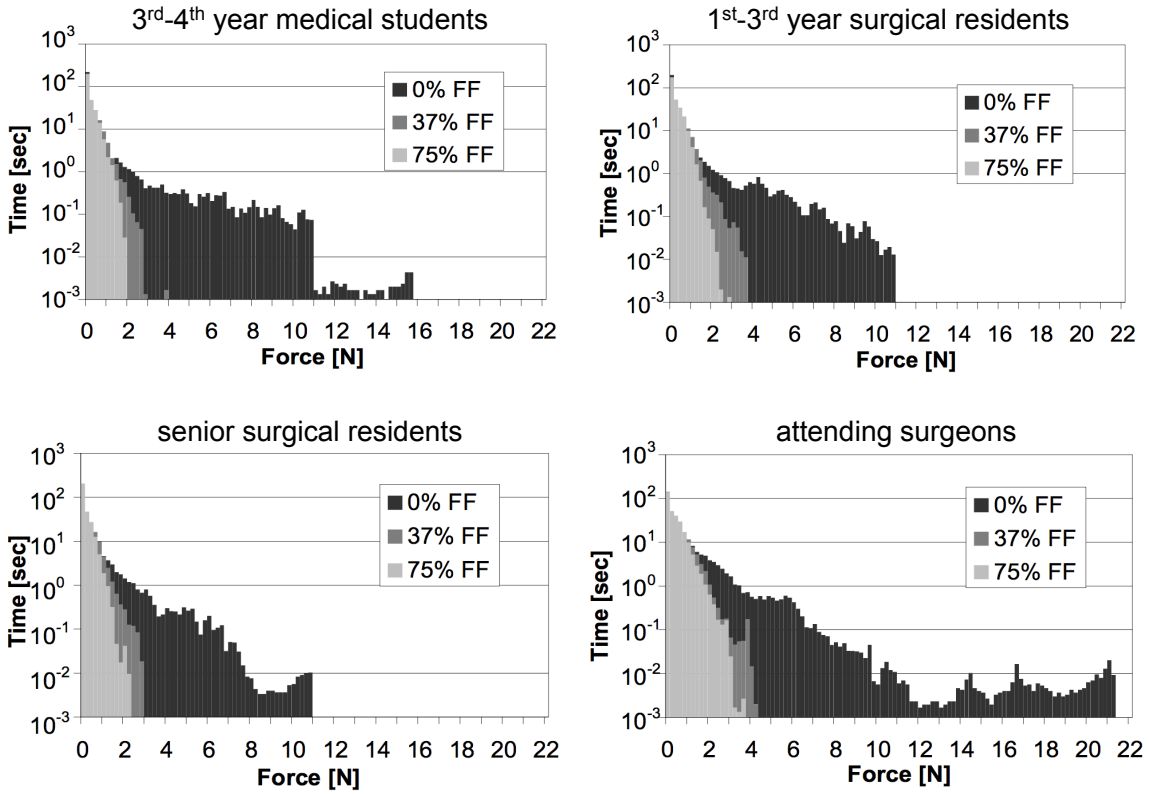

Figure 5. Plots representing the duration of applied load and the magnitude of the grasping force for four population groups during a phantom surgical task. Participants were asked to dissect a synthetic artery from synthetic tissue in five minutes. The magnitude of the applied force during this surgical task was elevated in the absence of force feedback (FF). Increasing the feedback gain resulted in lighter and longer application of force. Adapted from [19]].

The cumulative results of each population group are presented in Figure 6. For each metric (root mean square of application force, peak force, and the number of surgical errors) the addition of force feedback resulted in improvements in the surgical task for each population group. Moreover, additional improvements (e.g. lower forces) were introduced with larger feedback gain. The plot representing length dissected indicates that the addition of force feedback does not result in slower dissections.

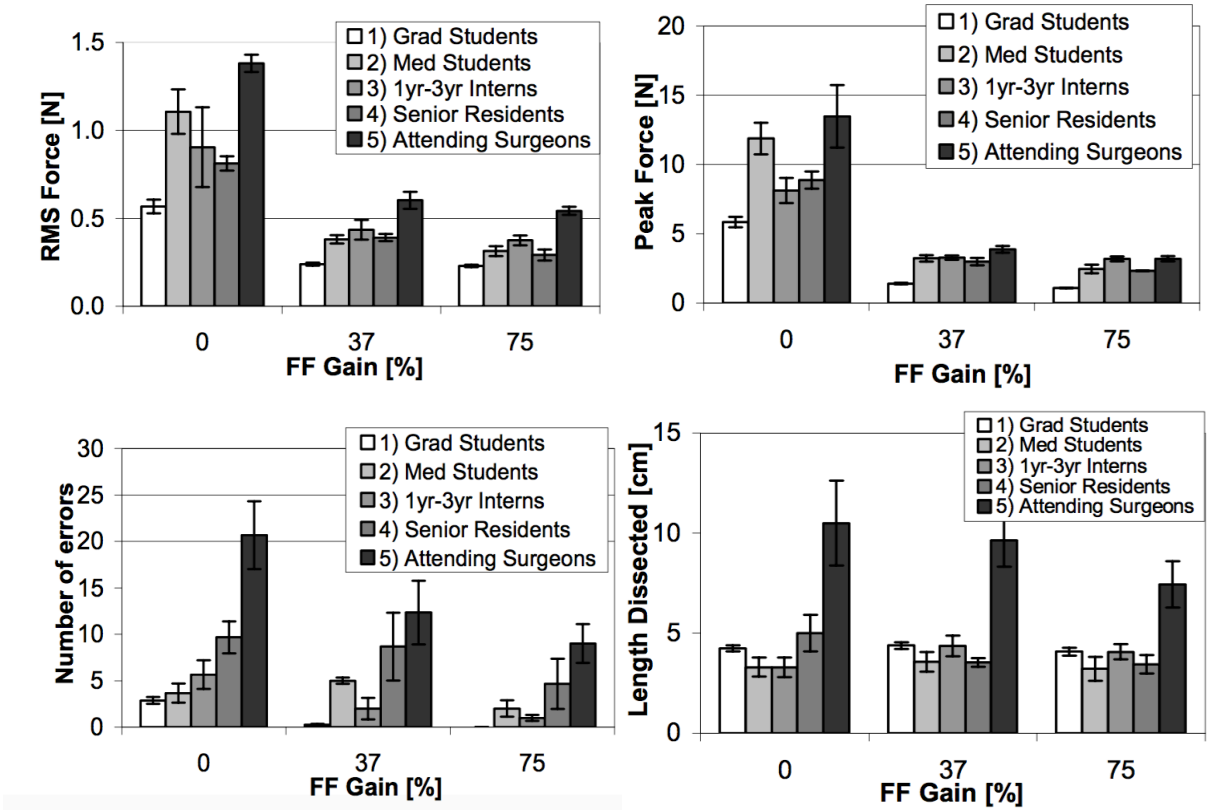

Figure 6. Plots representing the root mean square of force, peak force, number of errors, and length dissected for each population group as a function of the force feedback gain. For each

metric, the addition of force feedback resulted in improvements in the surgical task. The length dissected plot represents a performance metric demonstrating that the addition of force feedback did not result in slower dissections.

This study demonstrates that force feedback will result in lower applied loads, fewer errors, and without an increase in the duration of surgical tasks. Separate studies have also shown that traditional laparoscopic surgery and robot-assisted laparoscopic surgery, without force feedback, can lead to higher prevalence of suture rupture and premature suture failure, both intra- and postoperatively. Therefore, one can conclude that the addition of tactile feedback to laparoscopic and robotic laparoscopic systems can reduce intraoperative complications and result in improved patient outcomes.

1.5 Prior Art (maybe move to design chapter, before our design)

Research groups have previously attempted to integrate sensors with minimally invasive surgical graspers. To date, these sensors have been integrated on the instruments in locations both inside and outside the body, utilizing different sensing modalities to capture the tissue-instrument interface. Sensor integration to different grasper regions offers unique advantages (Section 2.1).

Stephen's et al. recently developed a system to estimate surgical loads based on interpretation of the torque and position of the surgical arm [20]. The sensor was designed to integrate to the proximal end (handle) of the da Vinci surgical grasper and interface with the spindles responsible for control of the grasper jaws. The authors argue that modifications to the handle, and not to the grasper, will expedite transition into the operating room.

Sie et al. developed a similar “tissue aware” system capable of tissue identification and prevention of crush forces [21]. This system relies heavily on estimation, is sensitive to initial conditions, and requires complex tissue identification algorithms and a database of tissue properties.

Lee presented work on a sensor implemented on the grasper wrist of a Raven II surgical system and torque sensors on the driving pulleys [22]. This sensor is capable of multi-axis force estimation, which estimates the surgical loads based on a capacitive sensor system that does not come in contact with the tissues during surgery.

Ahmadi developed an optical system that was integrated with the end-effector of the surgical grasper [23]. The magnitude and position of the load modulated the coupling efficiency. The sensor is capable of detection of different anatomical features including lumps and arteries during robotic tasks and does not interfere with electrical components due to the all-optical nature of the device.

Kim et al. developed a novel capacitive sensor integrated into the distal end of the grasper. The sensor requires machining of the grasper tip to provide shear and compression data to the surgeon. The design allows for simple detection of several load vectors with a minimum number of electrode elements [24, 25].

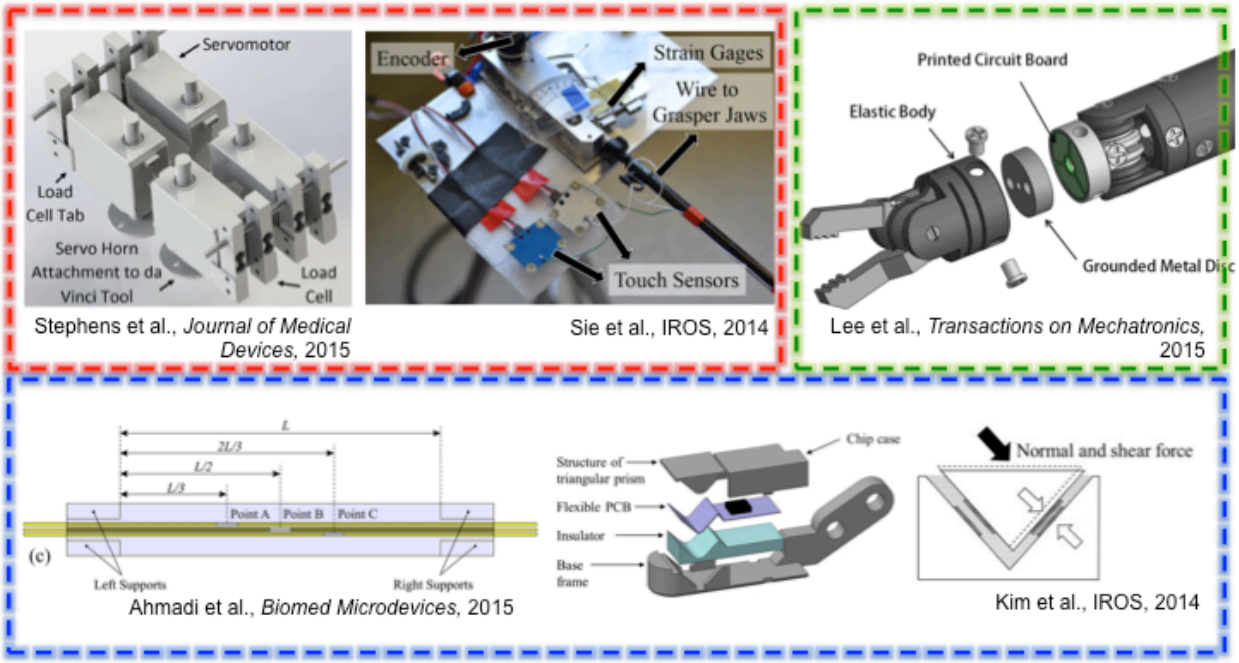

Figure 7. Surgical sensor system prior art. Here the red outline represents sensors located at the grasper handle; green represents a sensor solution in the grasper shaft; and blue represents sensor solutions integrated at the grasper tip. Research groups have proposed different sensing modalities, including optical sensing, capacitive sensing, and force estimation based on servo output.

Chapter 2 **Design**

2.1 Sensor Location

Attempts have been made to integrate sensors on surgical graspers previously. Focusing solely on robotic surgical systems, four grasper regions have been identified as possible integration sites of sensor systems, Figure 8.

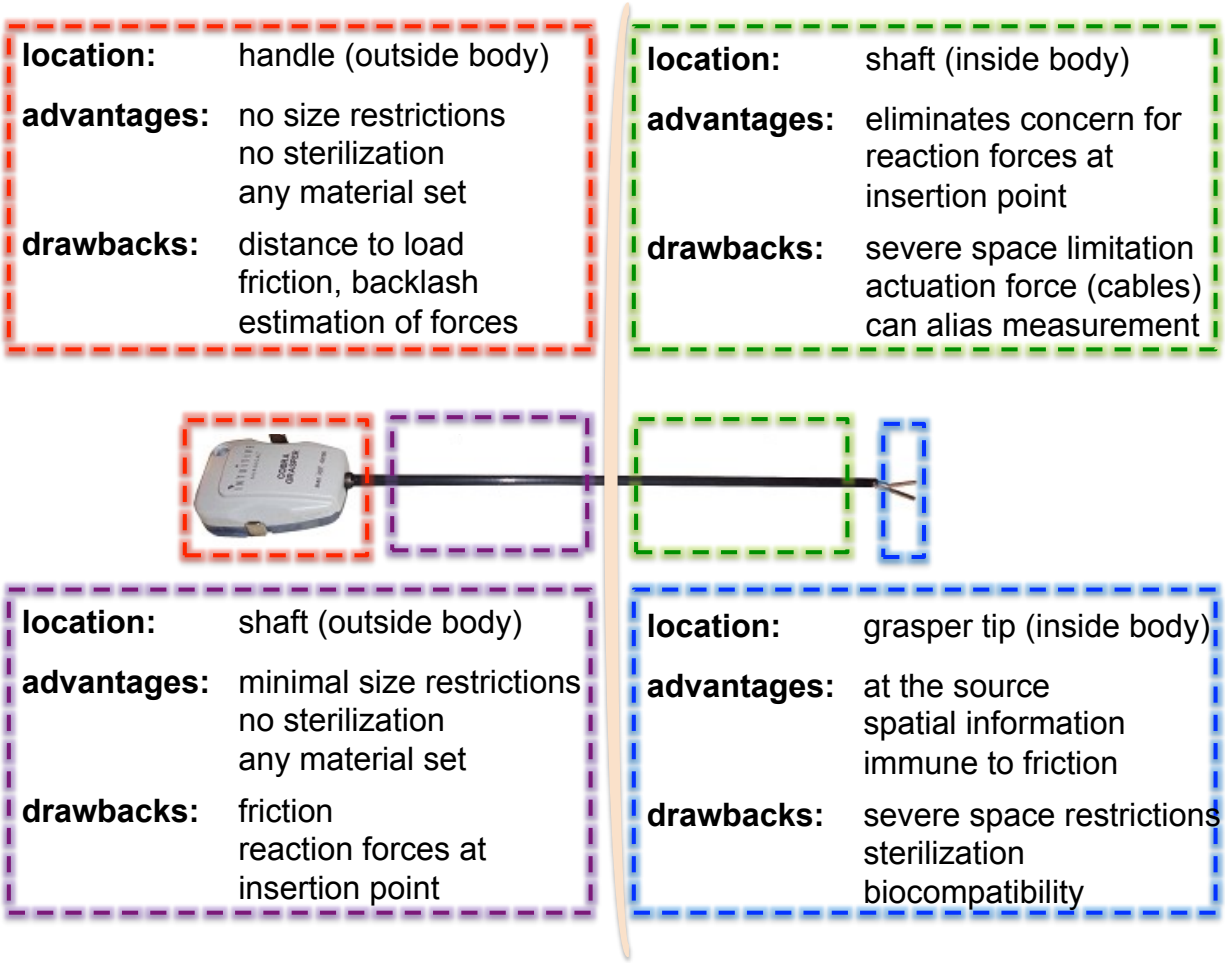

Figure 8. Locations on the robotic grasper that have been identified as possible locations for sensor systems. Each region is characterized by advantages and disadvantages. Different research groups have implemented sensor solutions in every region. Beige arc in the center of the figure represents the abdominal cavity where regions to the left are outside the body and those to the right are inside the body. [26]

Generally, solutions can be classified as *inside* or *outside* the body. Those systems that are located outside the body are not restricted by size, material, or sterilization requirements. Conversely, sensors that are intended to be located inside the body (e.g., on the distal end of the shaft or directly on the grasper tip) require a small form factor, selection from biocompatible material sets, and sterilization prior to surgery.

Although there are fewer restrictions when the sensor is placed outside the body, the challenge is that the load is always applied at the grasper tip. This distance creates issues with friction, backlash, reaction forces at the insertion point, and ultimately results in an *estimation* of the actual gripping forces as opposed to a direct measurement. Moving the sensor into the body, but away from the grasper tip surface, still requires estimation and potential distortion due to the actuation forces of the cabling.

The most accurate representation of the loads during surgery can be captured with sensors integrated on the grasper tip. Placing a sensor in this region necessitates the smallest sensors because of the severe size restrictions. This work focuses on tip-integrated technologies for three reasons: delicate surgical tasks require accurate measurements, which cannot be distorted by the cabling or estimated based on motion of the robotic arm; palpation, which is necessary to discern texture, size, and tissue boundaries, would require direct tissue-sensor interaction; and, sensors integrated on the tip can be arrayed and therefore provide better spatial resolution.

Table 3. Tip-integrated sensor technologies

Sensing modality	Modulated parameter	Sensor advantages	Sensor disadvantages
Piezoresistive	Resistance change	High spatial resolution High scanning rate	Hysteresis Low repeatability Significant drift
Piezoelectric	Strain polarization	High frequency response High dynamic range	Poor static sensing
Optical	Light intensity Spectrum change	Good sensing range Reliable Repeatable	Bulky Non-conformable
Capacitive	Capacitance change	Excellent sensitivity Large dynamic range Good spatial resolution	Complex electronics Noise susceptibility

Knowing the space limitations, sensing modalities with characteristics that meet the requirements were considered and tabulated (Table 3). Specifically, piezoresistive, piezoelectric, capacitive, and optical sensors were each considered. Because the sensors from each of the sensor modalities were capable of sensing over the required dynamic range and with the sensitivity required for surgical applications, the largest determinant of an appropriate sensing modality was assigned to *sensor disadvantages.*

Briefly, the disadvantages of a capacitive sensing modality are primarily associated with the interfacing electronics and noise susceptibility, both of which are not an inherent property of the sensor and can be controlled with appropriate shielding, circuit design, and printed circuit board (PCB) layout. Therefore, the decision was made to design and fabricate a capacitive sensor for normal and shear force detection and quantification.

2.2 Performance Criteria

The following paragraphs describe the decision-making processes involved in determining the appropriate geometric profile and performance metrics required for detection of the typical (and maximum) loads during surgical procedures with the required sensitivity and time resolution required for real-time sensing.

2.2.1 **Sizing**

Cutaneous mechanoreceptors that respond to mechanical stimuli are distributed unevenly over the body, including the finger pads. These receptors have a receptive field, the size of which is dictated by the location on the body and the relative density of mechanoreceptors at that location. In the finger pads, the average receptive field diameter, determined by the two-point discrimination test, is 2-4 mm (Figure 9).

Logically, element dimensions larger than the receptive field diameter, when mapped back to the surgeon's hand can result in reduced spatial resolution. Correspondingly, sensor elements that are designed with dimensions much smaller than the receptive field diameter, when mapped back to the surgeon's hand, will result in unnecessary computational complexity without an advantage, as the spatial information will be lost at the tactile display when transferred to the surgeon's finger pads. Specifically, when multiple stimuli trigger the same receptive field, the finger interprets that as a single stimulus. Importantly, this size restriction applies for both the compressive as well as shear sensing elements. It is noted that the 2-4 mm spacing is at the surgeon's fingertips, and that sensors closer together can be useful as long as they are mapped to the ideal spacing at the surgeon's hand.

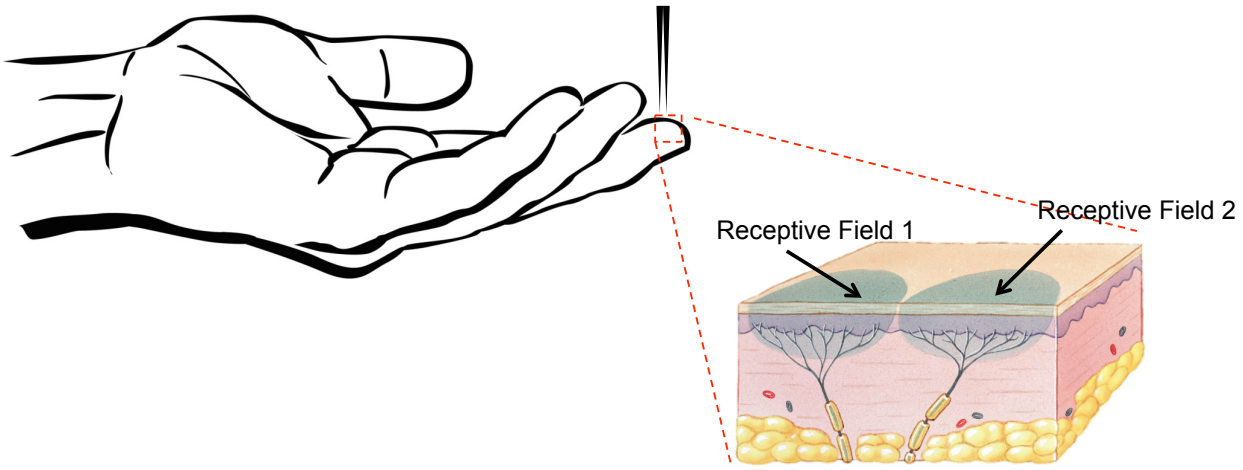

Figure 9. Mechanoreceptors on the finger pads. Each receptive field feeds back information from mechanical stimuli to the corresponding receptor. The size of the receptive field dictates the size of the sensor elements. Too large, and the sensor will trigger multiple receptive fields. Too small and tactile information will disappear at the tactile display. Adapted from M. J. Malachowski's schematic.

2.2.2 **Sensitivity and Dynamic Range**

Information relayed from the sensor to the tactile display must also be bound by the finger's detection limits. More clearly, as a species, humans are capable of detecting loads of 0.1 mN on the finger pads, and forces smaller than this may not register a response from the mechanoreceptors. Yet, it takes forces an order of magnitude larger such that localization of the applied load becomes possible. This fact is important because the output of arrayed sensors, which would give better spatial resolution for tactile sensing and tissue palpation, must be capable of being localized on the finger pad to give meaningful results. Although the contact forces can be scaled between the sensor and the surgeon, these two numbers define the lower bounds of the sensor sensing range – force magnitudes below this threshold, without scaling, will not register a response at the surgeon's fingertips. Conversely, the upper end of the dynamic range

is defined by the maximum loads experienced during laparoscopic surgeries. From consultation with subject matter experts, this upper bound has been reported to hover around 20 N, although loads exceeding ~14 N (285 kPa over a 56.4 mm^2 grasper area) result in tissue injury. [17] Therefore, to cover the entire dynamic range of forces experienced during typical minimally invasive surgery the sensor must be designed to respond with adequate sensitivity. Yet, although the finger is capable of detecting and localizing sub-Newton loads, our perception of such small loads is crude. More specifically, the typical subject cannot discern a difference between, for example, 1 mN and 10 mN or 100 mN and 150 mN. It's not necessarily essential that the tactile display relay the exact load profile back to the surgeon, but rather a simpler output of binned force ranges can be more meaningful.

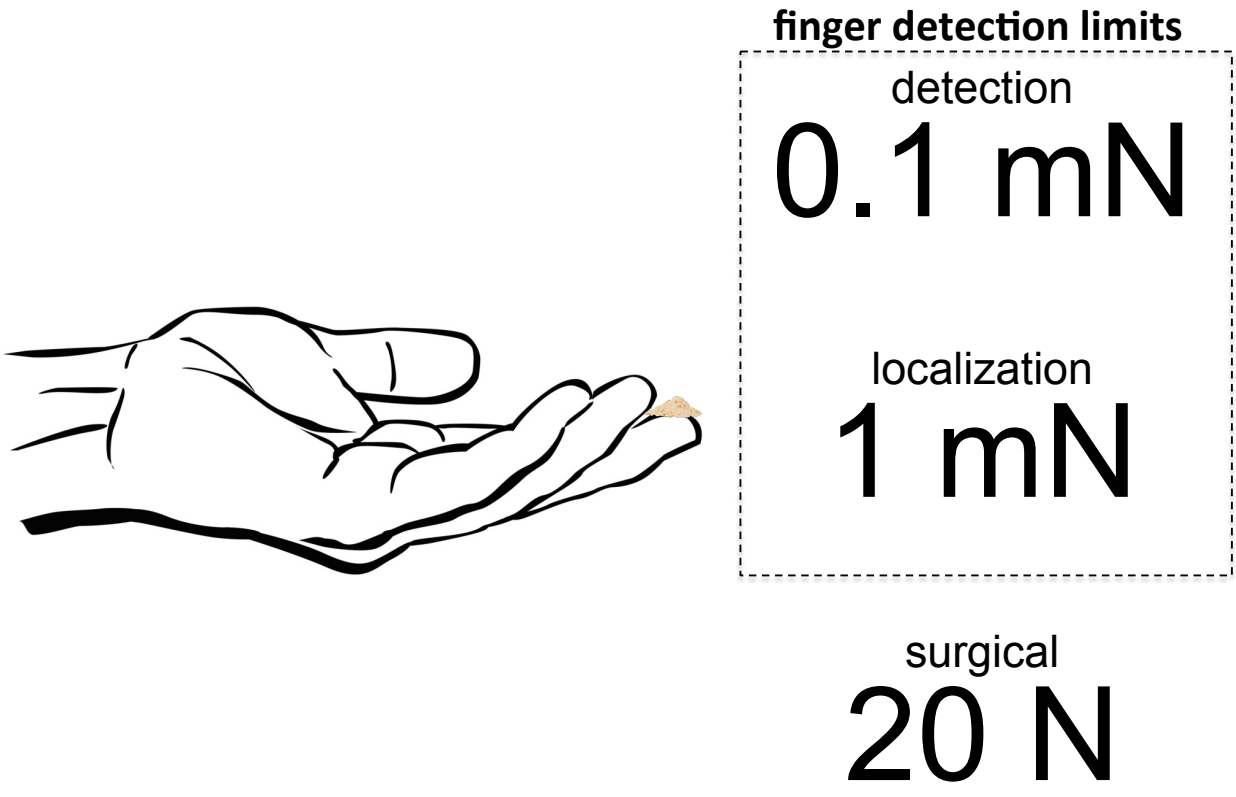

Figure 10. The finger detection limits and the upper bound typical of laparoscopic surgery. The sensor must be capable of responding over the entire dynamic range (1 mN to 20 N) with adequate sensitivity to capture the tissue-grasper interaction over the course of a procedure.

2.2.3 **Temporal Resolution**

While the milliNewton output is not necessarily important for tactile feedback because of the surgeon's lack to discern such small changes, millisecond responses are critically important.

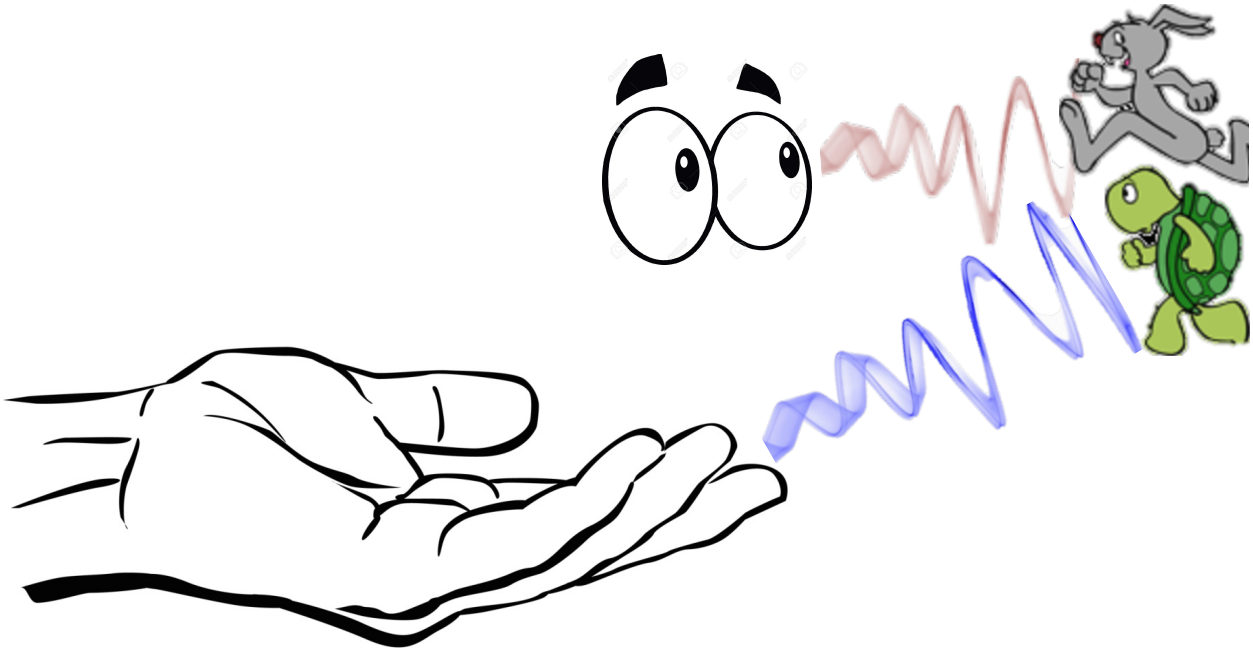

Figure 11. Cartoon representation of temporal resolution of tactile feedback system. The real-time visual feedback (hare to the cartoon eyes) must not precede the tactile feedback (tortoise to the fingertips) by more than 330 milliseconds. Delays exceeding this threshold result in distractions that impede instead of aid surgery.

The tactile information at the robot-tissue interface must be displayed to the surgeon in real time. The surgeon already has a real-time view of the surgical field through a stereoscope at the console, and the tactile feedback must accompany the movements they are seeing on the monitor. Excessive delays of tactile information, longer than 330

milliseconds, become distracting and disruptive [27]. It's critical for the entire feedback system, sensor, circuit, and tactile display to respond quicker than the maximum lag time.

2.3Working Principle

2.3.1 **Parallel Plate Capacitive Sensor**

The parallel plate capacitive sensor is designed to respond to compressive loads. The area of the sensor elements determines the overlap area, and the dielectric gap is a function of the applied load, where surgical loads create a relative decrease in the gap between the top and bottom electrode, and therefore an increase in the capacitance.

2.3.2 **Combined Compressive and Shear Sensor**

Illustration of the sensor layout helps explain the working principle of the combined compressive and shear sensor. The sensor is designed as a single-sided capacitive sensor for simpler integration with electronics and the surgical grasper. The single-sided sensor architecture allows for soldering the sensor directly to the printed circuit board and eliminates frail wirebonds. In addition to the integration, the design was motivated by a need protect the sensor surface from sterilization and surgical environments while allowing for accurate measurements of the tissue-grasper interface. Therefore, for both compressive and shear sensing, the measurement is made between capacitors in series combination. The upper half of the next three figures shows a top-view of the sensor, while the bottom half shows a side or cross-sectional view of the sensor through the cut line in the sensor midplane.

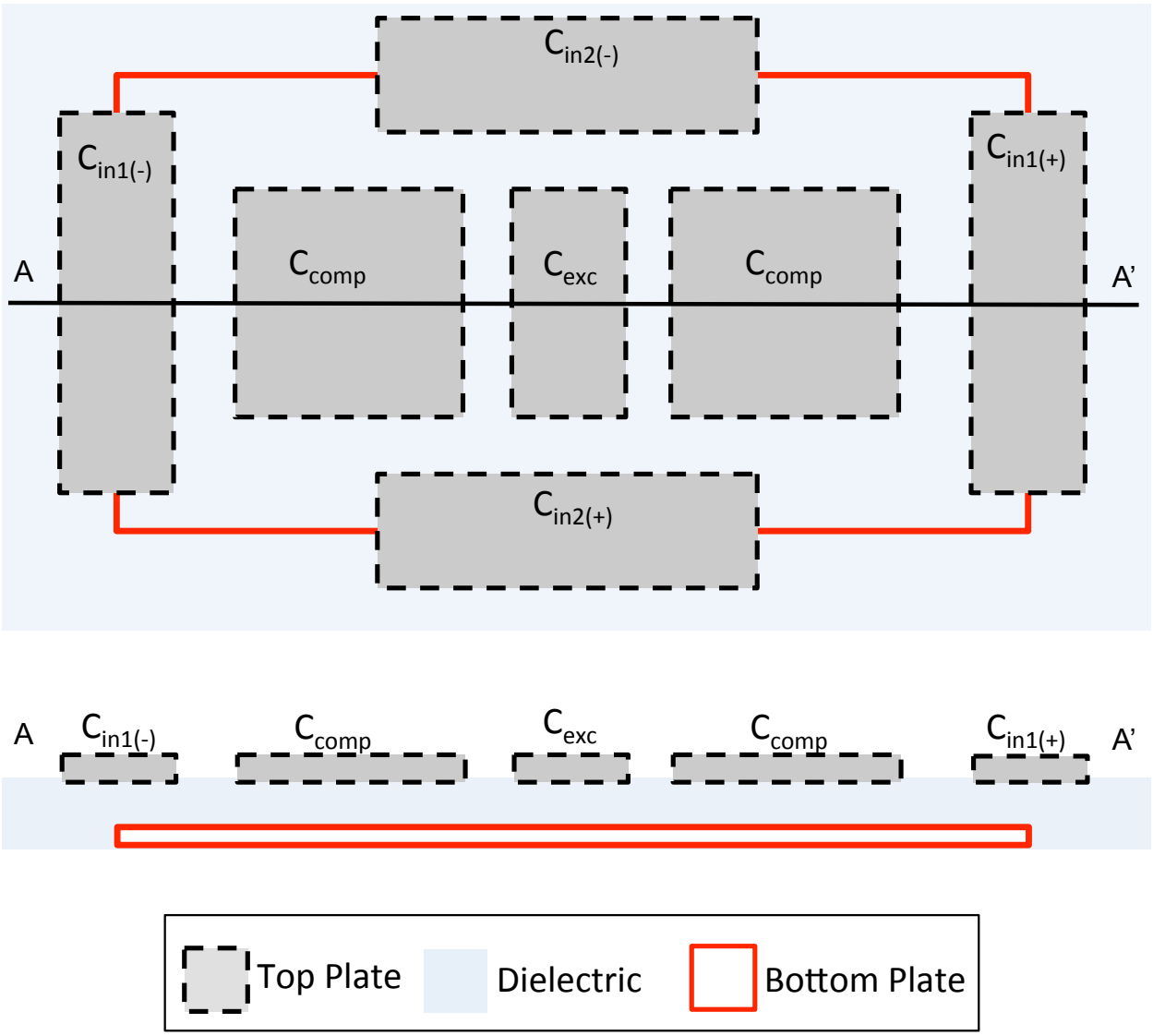

Figure 12. Schematic representation of the combined normal and shear sensor. The top plate, dielectric, and bottom plate are represented in top-view (top half) and cross section (bottom half) through the AA' line. The top metal plate consisted of 7 separate electrodes, two of which (C_{comp}) were required for compressive sensing and the remaining created the shear sensor.

The top metal is composed of seven separate electrodes. Compressive loads are captured by the two large squares left and right (C_{comp}) of the center electrode (C_{exc}) with the remaining perimeter electrodes ($C_{in1(+)}$,$C_{in1(-)}$,$C_{in2(+)}$,$C_{in2(-)}$) required for shear sensing in the both the lateral and transverse directions.

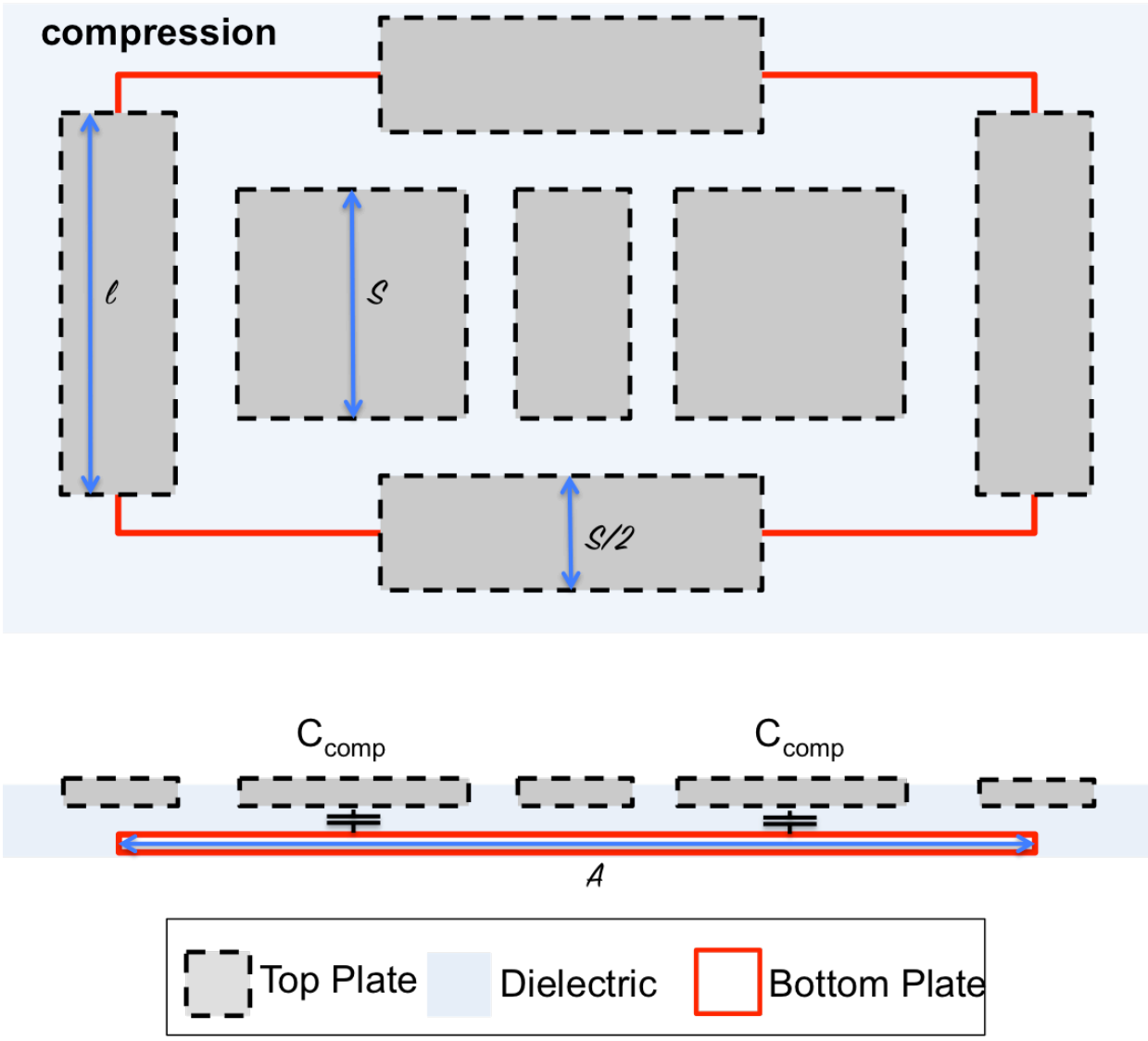

Figure 13. Combined sensor working principle in response to compressive load. When a compressive load was applied to the top plate of the capacitor, the gap between the top plate and bottom plate decreased resulting in an increase in the capacitance. The measured capacitance was the series combination of the two C_{comp} components through the bottom plate. Because the shear sensing is a differential measurement, no change is detected through the shear sensor elements.

Under purely compressive loads, the overlap of the top and bottom electrodes does not change, and therefore any change in capacitance is due to a decrease in the dielectric gap. The center electrodes, those responsible for compressive sensing, have

been designed such that under any load condition the overlap area will not change with the chosen material set. The signal is registered through the series combination of the two compressive electrodes. Importantly, this measurement is setup to be a single ended measurement. Because the shear sensing electrodes are designed make a differential measurement, uniform compression will not result in a registered shear measurement.

A shear load is applied in the +x direction (from left to right on the page) in Figure 14. In this case, no change in the overlap area occurs for any of the electrode elements except for the elements on the left and right of the figure. For a shear in the +x direction, the top electrodes collectively move to the right with respect to the stationary bottom electrode. This causes an increase in the overlap area of the left electrode and an equivalent decrease in the overlap area of the right electrode. For shear in the +y direction, or any other lateral or transverse shear, the same principle applies and the overlap areas of the perimeter electrodes vary based on the magnitude and direction of the shear load.

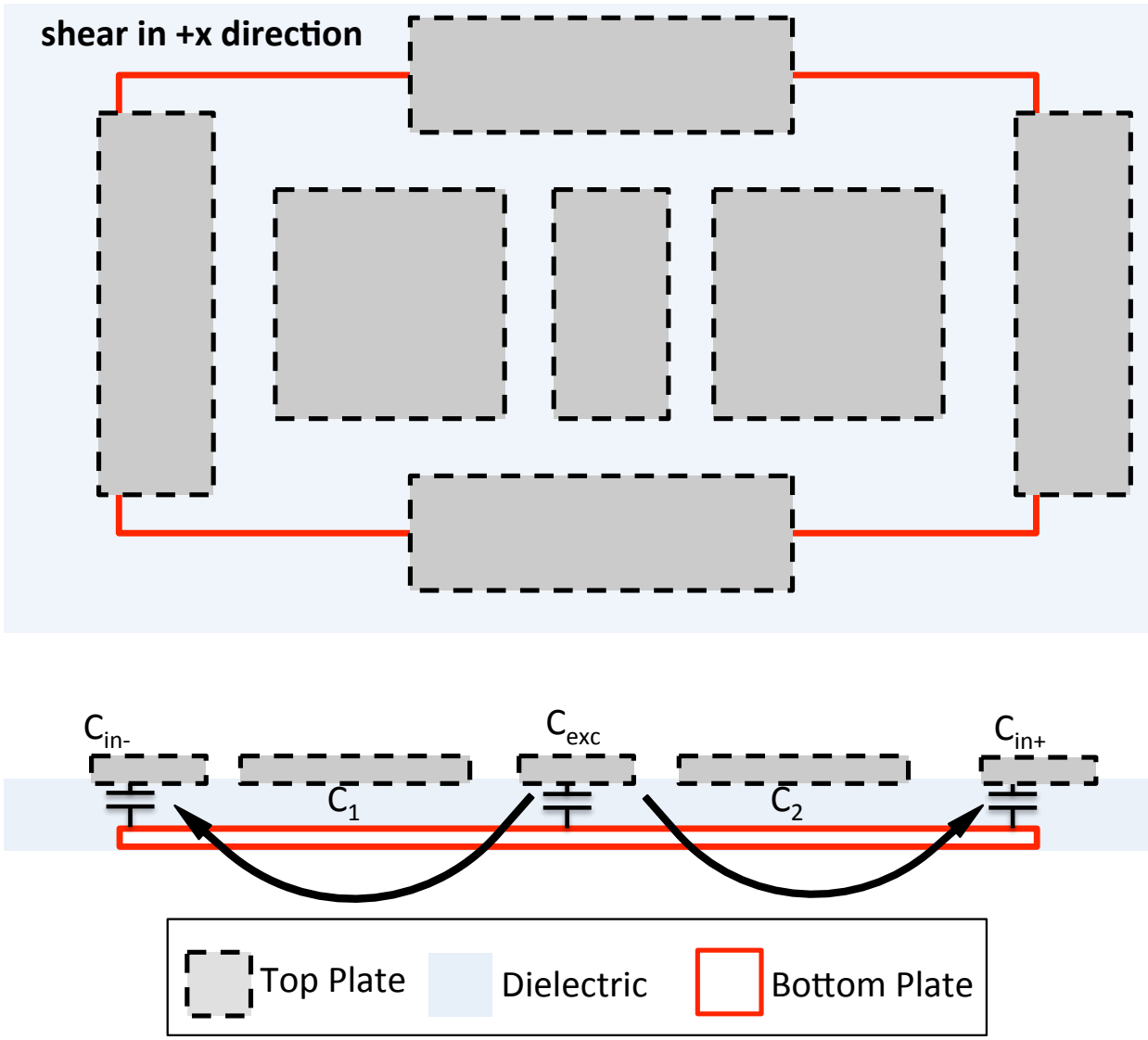

Figure 14. Combined sensor working principle in response to shear load in the positive x (from left to right) direction. A shear load causes a change in the overlap area. In the case of a shear load in the positive x direction, the elements translate to the right, which cause an increase in the overlap of the left element and a similar decrease in the overlap of the right element. This causes an increase in capacitance on the left and a decrease on the right and no change to the excitation capacitance (C_{exc}). The resulting shear load could be quantified by looking at the differential measurement, or change, due to the change in the overlap area. The same principle could be applied if the shear vector were in the y direction (top to bottom) or if the shear were applied at any arbitrary angle.

2.4 Theory

2.4.1 **Parallel Plate Capacitor**

Capacitance of a parallel plate capacitor is given by equation (1) ,where ε_o represents the permittivity of free space, ε_r is the dielectric constant, A_{plate} is the overlap area of the capacitive plate, and z represents the dielectric thickness, and fringe fields are assumed to be negligible.

$$C = \frac{\varepsilon_o \varepsilon_r A_{plate}}{z} \tag{1}$$

The stress-strain relationship of a linear elastic material is defined by equation (2) where E represents the elastic modulus of the material, σ is the stress, which can also be expressed as force (F) over area (A), and γ is the strain.

$$E = \frac{\sigma}{\gamma} = \frac{F/A}{\Delta z / z_o} \tag{2}$$

Rearranging equation (2) gives equation (4), where z is the same dielectric thickness found in equation (1) and z_o is the unperturbed thickness, equation (3).

$$\Delta z = z - z_o \tag{3}$$

$$z = (1 - \frac{F}{EA}) z_o \tag{4}$$

Inserting equation (4) into equation (1) yields an equation for the capacitance of a parallel plate capacitor as a function of an applied load, equation (5).

$$C = \frac{\varepsilon A_{plate}}{\left(1 - F/EA_{plate}\right) z_o} \tag{5}$$

For cases that satisfy equation (6),

$$\frac{F}{EA_{plate}} << 1 \tag{6}$$

a simplifying assumption can be made to reveal equation (7).

$$C \cong \frac{\varepsilon A}{z_o}(1 + \frac{F}{EA}) = \frac{\varepsilon}{z_o E} F + \frac{\varepsilon A}{z_o} \tag{7}$$

This linear approximation states that the capacitance in response to an applied load is the sum of the baseline capacitance, determined by the sensor geometry and a separate term that stems from the material properties and defines the sensitivity. For surgical loads and the designs described here, the approximation is valid.

2.4.2 **Combined Compressive and Shear Sensor**

2.4.2.1 Compressive Sensor Theory

The definition of a parallel plate capacitor is the same as defined in equation 1 above. However, for this combined sensor, because of the mounting orientation, the assumption is that the load will be applied to and distributed across the entire sensor surface, *A,* not only to the sensor elements in the top plate, where a side of the square

sensor is defined as *s,* the length of the perimeter electrodes are defined as *l,* and the width of the perimeter of the electrodes are defined as $\frac{s}{2}$ (Figure 13).

Here, compression is sensed as the series combination of two identical parallel plate capacitors (8),

$$C_{eq} = \frac{C_1 C_2}{C_1 + C_2} \tag{8}$$

and the equivalent capacitance (C_{eq}) is represented by equation (9).

$$C_{eq} = \frac{1}{2} C_1 = \frac{\varepsilon_o \varepsilon_r s^2}{2z'} \tag{9}$$

Substitution of equation (9) into equation (4) reveals the equivalent capacitance in response to an applied load (10).

$$C_{eq} = \frac{\varepsilon_o \varepsilon_r s^2}{2z(1 - \frac{F}{AE})} \tag{10}$$

Using a Maclaurin Series approximation, the sensor output can be defined by equation (11).

$$C_{eq} \approx \frac{\varepsilon_o \varepsilon_r s^2}{2z}(1 + \frac{F}{AE}) \tag{11}$$

2.4.2.2 Shear Sensor Theory

Because the change in capacitance in the shear sensing elements is due to a change in the overlap area and not a change in the dielectric thickness, the area terms must be defined. Here $\frac{s}{2}$ is the lateral dimension of the electrode, *l* is the length of the rectangular element, and *y'* is the amount of perturbation of the surface due to an applied shear

load. The sensor is designed such that half of the perimeter electrode is overlapping the bottom electrode, $\frac{s}{4}$.

The shear sensor is a measurement of the series combination of multiple electrodes, and also a differential measurement between two separate series combinations ($C_{1/2}$). The following equations will define the process to determine the effects of shear force in the *x-direction*, and due to symmetry, the same equations can be applied to understand shear in the *y-direction*.

Here, the capacitance is determined between positive and negative input capacitance terminals ($C_{in(\pm)}$) and an excitation terminal (C_{exc}), illustrated in Figure 14. The series combination is defined as equation (12).

$$C_{1/2} = \frac{C_{in1(\pm)} C_{exc}}{C_{in1(\pm)} + C_{exc}} \tag{12}$$

The area of the input capacitance terminals is defined as equation (13),

$$A_{in1(\pm)} = (\frac{s}{4} \pm y')l \tag{13}$$

and the area of the excitation terminal is defined as equation (14)

$$A_{exc} = \frac{sl}{4} \tag{14}$$

Capacitance C_1 and C_2 can be defined as equations (15) and (16), respectively. Also, the terms for the relative permittivity and permittivity of free space have been combined into a single permittivity term, ε.

$$C_1 = \frac{(\frac{\varepsilon A_{exc}}{z})(\frac{\varepsilon A_{in1(-)}}{z})}{(\frac{\varepsilon A_{exc}}{z}) + (\frac{\varepsilon A_{in1(-)}}{z})} = (\frac{\varepsilon}{z})(\frac{A_{exc} A_{in1(-)}}{A_{exc} + A_{in1(-)}}) \tag{15}$$

$$C_2 = \frac{(\frac{\varepsilon A_{exc}}{z})(\frac{\varepsilon A_{in1(+)}}{z})}{(\frac{\varepsilon A_{exc}}{z}) + (\frac{\varepsilon A_{in1(+)}}{z})} = (\frac{\varepsilon}{z})(\frac{A_{exc} A_{in1(+)}}{A_{exc} + A_{in1(+)}}) \tag{16}$$

To create the differential output (C_x), equation (16) is subtracted from equation (15) to yield equation (17).

$$C_x = C_1 - C_2 \tag{17}$$

This creates equation (18), expanding the terms.

$$C_x = \frac{\varepsilon A_{exc}^2}{z}(\frac{A_{in1(-)} - A_{in1(+)}}{(A_{exc} + A_{in1(+)})(A_{exc} + A_{in1(-)})}) \tag{18}$$

Inserting equations (13) and (14) into equation (18), yields equation (19), which defines the differential capacitance in the x direction.

$$C_x = \frac{\varepsilon}{z}(\frac{sl}{4})^2(\frac{2yl}{(\frac{sl}{2})^2 - (yl)^2}) \tag{19}$$

Simplifying (19), gives (20)

$$C_x = \frac{\varepsilon}{2z}(\frac{s^2 ly}{s^2 - 4y^2}) \tag{20}$$

To determine the perturbation to the applied load, equation (21) relates shear stress to shear strain.

$$\tau = \frac{F}{A} = \gamma G = \frac{y}{z} G \tag{21}$$

Here τ represents the shear stress, γ the shear strain, and G represents the shear modulus. The force and area terms are identical to their definitions above. Substituting the shear modulus with an identical term relating Poisson's ratio and elastic modulus, *E*, in equation (22),

$$G = \frac{E}{2(1+\upsilon)} \tag{22}$$

yields equation (23),

$$y = \frac{2Fz(1+\upsilon)}{AE} \tag{23}$$

where the perturbation is described in terms of the geometry of the sensor, magnitude of the force applied, the elastic modulus of the material and the Poisson ratio. Combining equation (23) with equation (20) yields the shear sensing equation, equation (24)

$$C_x = \frac{\varepsilon l(1+\upsilon)}{AE} F \tag{24}$$

The theoretical response to a compressive load of the combined sensor is presented in Figure 15. A simplified linear approximation (dashed) and the analytically calculated

capacitance response to an applied load are presented for different fabrication layouts and dielectric thickness. The main take away from the calculation is that sensitivity increases for larger electrode dimensions or if the gap between the top and bottom electrode is minimized.

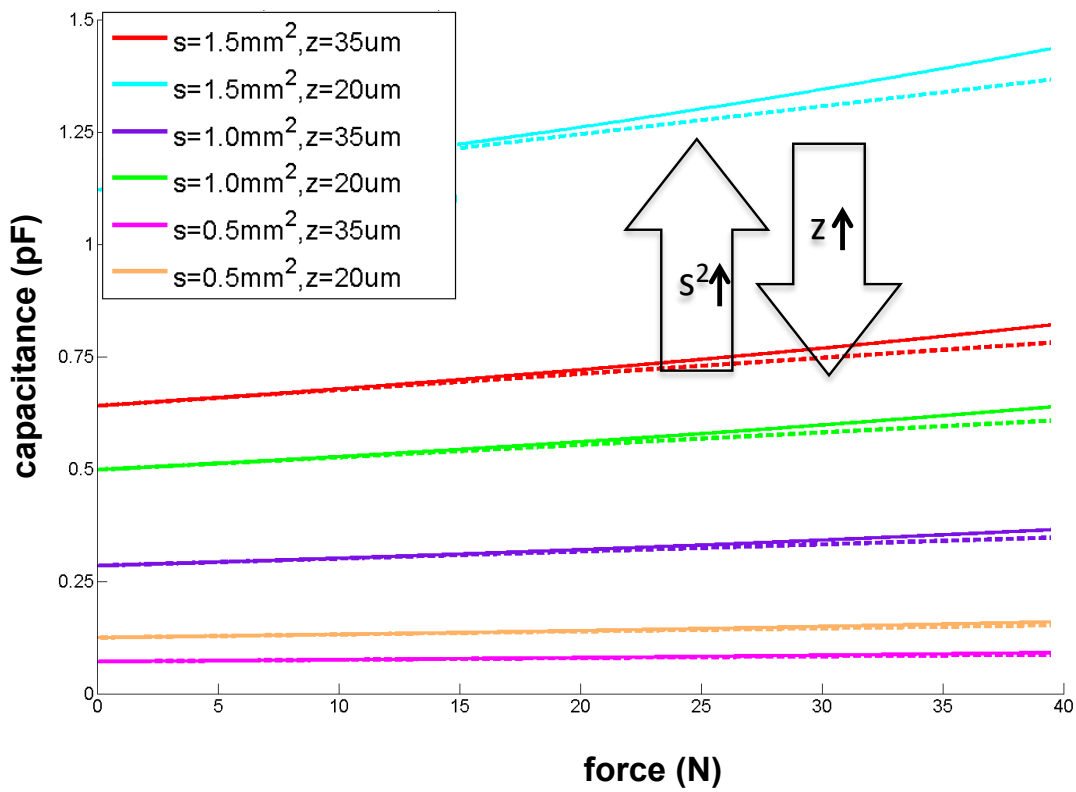

Figure 15. Calculation of the *compressive* output response of different second-generation capacitor designs in response to applied load. The main take away is the sensitivity (slope) increases with larger capacitive plates and by decreasing the initial gap between the top and bottom electrodes. The solid lines represent the analytical solution without simplifying assumptions, while the dashed lines represent the linear approximation.

This sensitivity is presented as the slope of the traces. For loads less than 20 N, (the majority of surgical loads) the linear approximation represents the capacitive output well, but the linear approximation is no longer valid for larger loads. For a sensor with a 1-

mm^2 overlap area and a 35 micron dielectric thickness, this sensitivity is calculated to be 3 femtoFarad/N. This model assumes a dielectric with an elastic modulus of 1 MPa, and relative permittivity of 2.5. Importantly, the x-y dimensions of the sensor cannot be made too large (integration with the grasper becomes more difficult and there exists a potential for two-point discrimination issues), but the thickness of sensor can be modified for various surgical needs. If the need is for an extremely sensitive sensor, the thickness can be decreased. If the need is for a larger dynamic range, however, the thickness can be modulated for that purpose as well.

The same analytical calculation was made for the shear-sensing component. Here the change in capacitance is due to a change in the overlap area. This measurement is a differential measurement where initially, with no load applied to sensor, the differential is set to 0 capacitance. If there are any fabrication misalignments, it is possible that the shear elements do not have equal overlap, and the unloaded condition is at a non-zero baseline value. Essentially, if a load is applied in the positive and negative direction, the sensor will output a positive and negative differential capacitance, the magnitude of which will be proportional to the magnitude of the shear load. For different elastic moduli, the sensitivity of the sensor is given in Figure 16. The lower the elastic modulus, the more sensitive the sensor to shear loads. Here for the following sensor parameters, the sensitivity is defined as 1 fF/N.

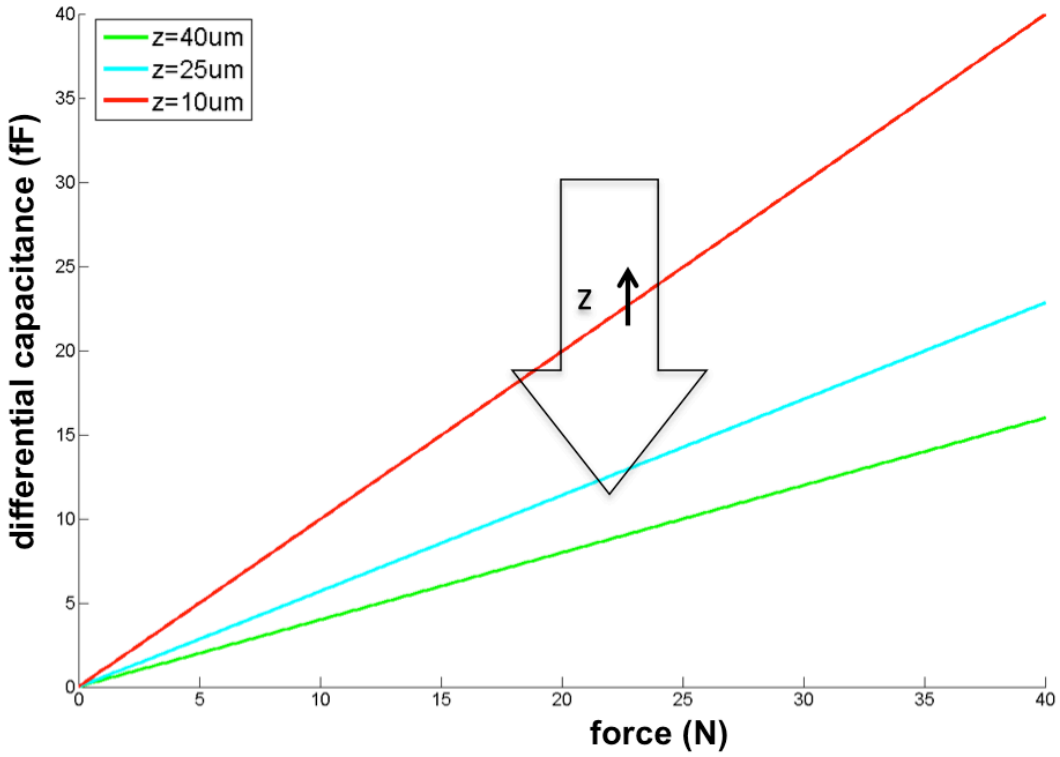

Figure 16. Calculation of the shear output response of different second-generation capacitor dielectric thicknesses in response to an applied shear load. The main take away is the sensitivity (slope) increases with a decreasing dielectric gap. Because the shear capacitance measurement is a differential measurement, in the absence of an applied load, the expected output would be 0 F. Shear in one direction would result in a positive differential capacitance and shear in the opposite direction would result in a negative differential shear.

Chapter 3 **Fabrication**

3.1 Microfabrication

Two sensor designs were microfabricated. Initially, a simple parallel plate capacitor was designed to sense uniaxial compression at the grasper-end of conventional laparoscopic tools. A second sensor design was subsequently developed to integrate shear sensing to detect intraoperative slipping and pulling of tissues. The design of the second sensor makes sensing of biaxial loads possible in addition to having all electrical contacts on one side for improved ease of integration with the surgical instrument.

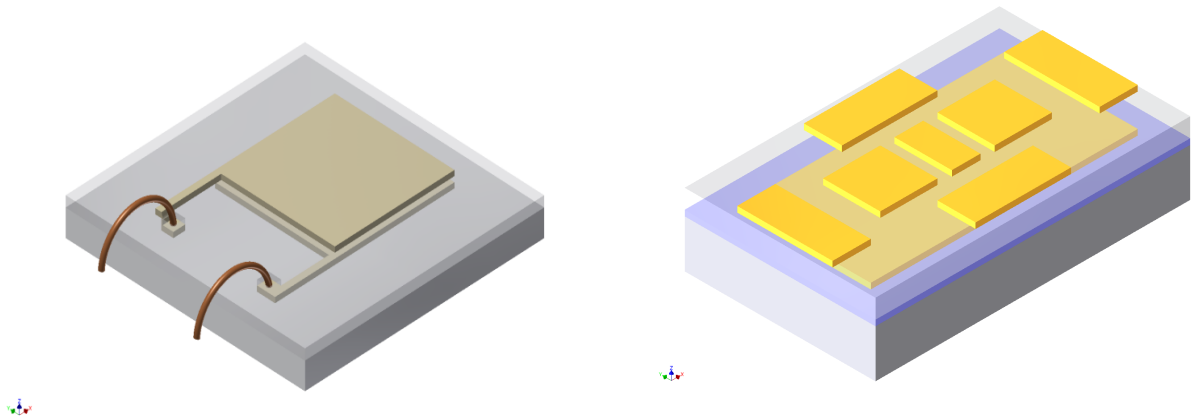

Figure 17. Two generations of capacitive sensors. (left) The single sensor element is capable of detecting typical surgical compressive loads. Compression results in a smaller gap between the top and bottom plates and therefore an increase in capacitance, which could then be used to determine the magnitude of the deflected load. (right) The combined compression and shear sensor. The compression can be sensed with a change in the dielectric thickness, while a change in the overlap area of the perimeter electrodes allow for detection and quantification of shear loads.

3.1.1 **Parallel Plate Capacitor**

The parallel plate sensors were fabricated on 100-mm diameter glass substrates. The substrates were cleaned using a 3:1 mixture of concentrated H_2SO_4 to 30% H_2O_2 (piranha solution) to remove organic residue and contaminants. The bottom electrode was first photolithographically patterned to define the 2D layout and coated with a 15-nm-thin adhesion layer of titanium (Ti) and a 1-micrometer-thick gold (Au) structural layer via electron beam evaporation. A lift-off process exposed the final profile of the bottom electrode. A 1-micron dielectric, Parylene C, was deposited by chemical vapor deposition (CVD) to separate the top and bottom electrodes. Vias were etched through to the bottom metal electrode using a reactive ion etcher (RIE) to selectively etch the exposed Parylene C. The top metal was patterned and defined identically to the bottom electrode and electrical connections were made to the sensor through a conventional wire bonding process. These microfabricated sensors were manufactured in arrays to give the surgeon spatial information of the surgical environment and a better picture of the interactions at the tissue-grasper interface.

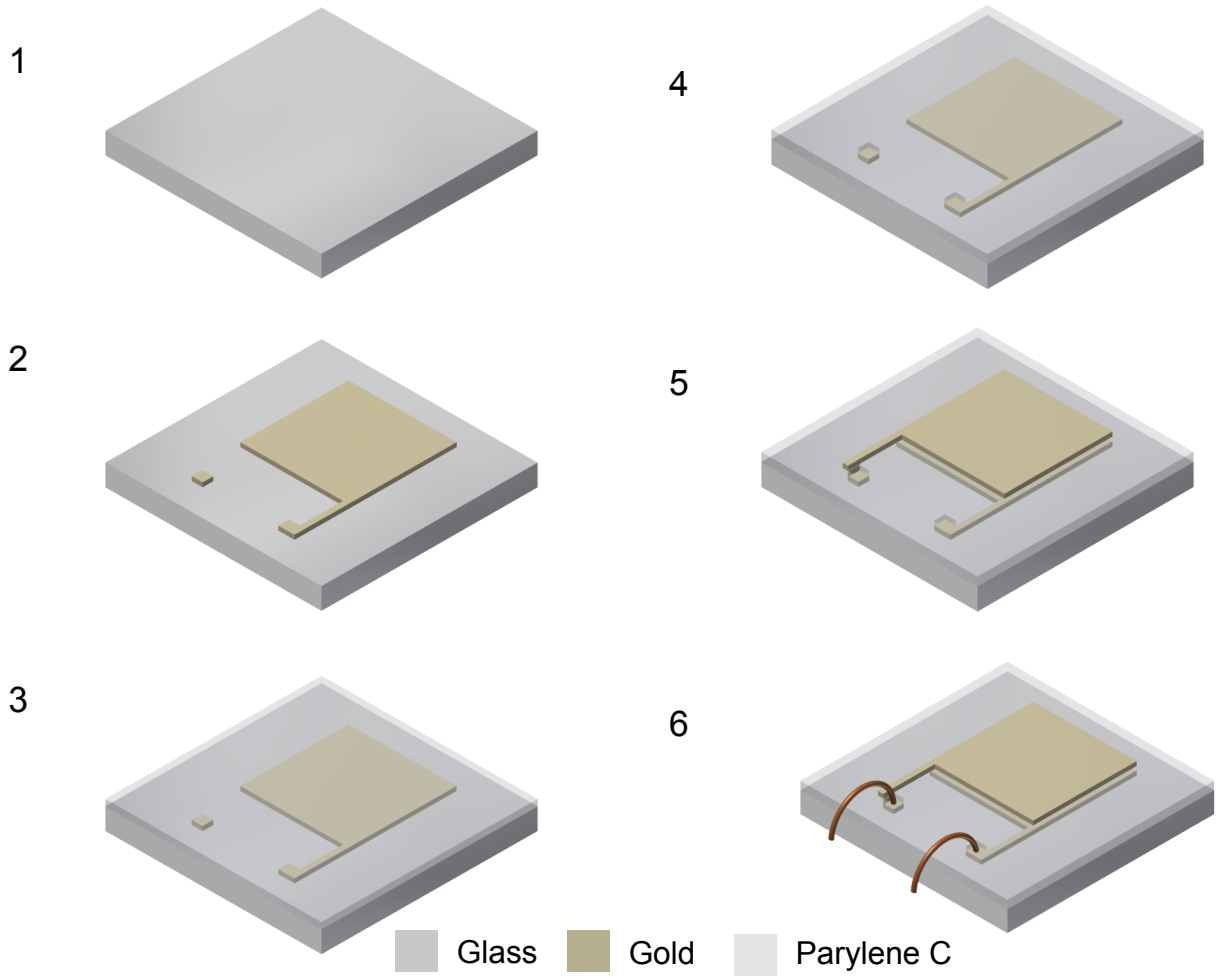

Figure 18. Fabrication steps for the parallel plate capacitive sensor. (1) Fabrication began with a single 4-inch glass wafer. (2) The bottom electrode was formed by an electron-beam-evaporated metal layer and lift-off of a previously developed photoresist. (3) The dielectric layer was formed by a chemical vapor deposition (CVD) of a 1-micron layer of Parylene C. (4) Vias were selectively etched into the dielectric with a reactive ion etch (RIE) process to create access to the underlying metal layer. (5) A second evaporation step and lift-off defined the top metal electrode. (6) The integration with the read-out circuit was accomplished with wire bonding to the sensor bond pads.

The final fabricated device has sensor elements that are arranged in arrays that can provide spatial information of grasping tasks when mapped to a similar tactile

display. Each sensor could serve as input to a separate pneumatic actuator on a tactile display.

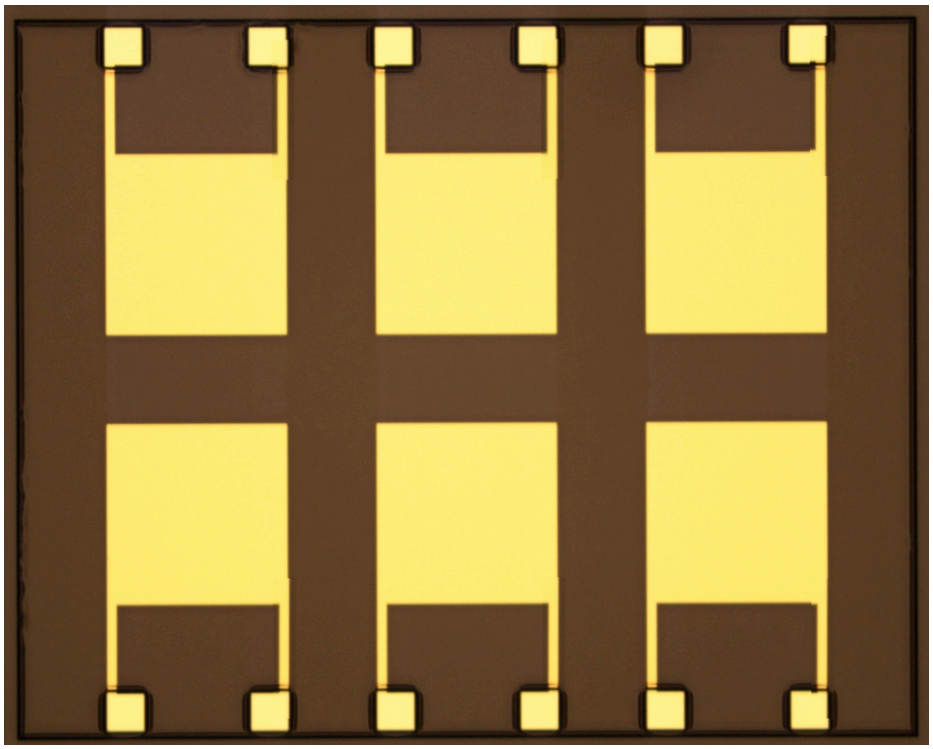

Figure 19. Final first-generation fabricated sensor array. A representative 3x2 array of 1-mm^2 sensors is presented. Dark edges outline areas where the Parylene C have been selectively etched away, including areas over the bond pads and lanes between adjacent sensor arrays.

3.1.2 **Combined Compressive and Shear Sensor**

Fabrication of the second-generation sensor began on blank silicon wafers. The substrates were cleaned using a 3:1 mixture of concentrated H_2SO_4 to 30% H_2O_2 (piranha solution) to remove organic residue and contaminates. A thermal oxidation process grew a 500-nm-thick silicon dioxide to electrically isolate the elements from the underlying substrate. The bottom metal was photolithographically defined with photoresist and a thin titanium/gold layer was evaporated onto the patterned substrate. Lift off of the photoresist revealed the patterned bottom metal. The dielectric, a 10:1

polydimethylsiloxane (PDMS) was spun on to the wafer and cured at elevated temperature. The dielectric thickness was previously calculated to achieve an appropriate sensitivity and dynamic range for surgical applications. A photoresist patterning step was developed for processing on the PDMS polymer without damaging the fragile elastomer during photoresist exposure or development because issues with adhesion and cracking were encountered on dummy wafers prior to processing of device wafers. The change from Parylene C to PDMS was made to accommodate the shear-sensing component. The stiffer Parylene C (2.8 GPa Young's Modulus), results in a shear sensitivity that is three orders of magnitude lower than a PDMS dielectric (1 MPa Young's Modulus) (Figure 16).

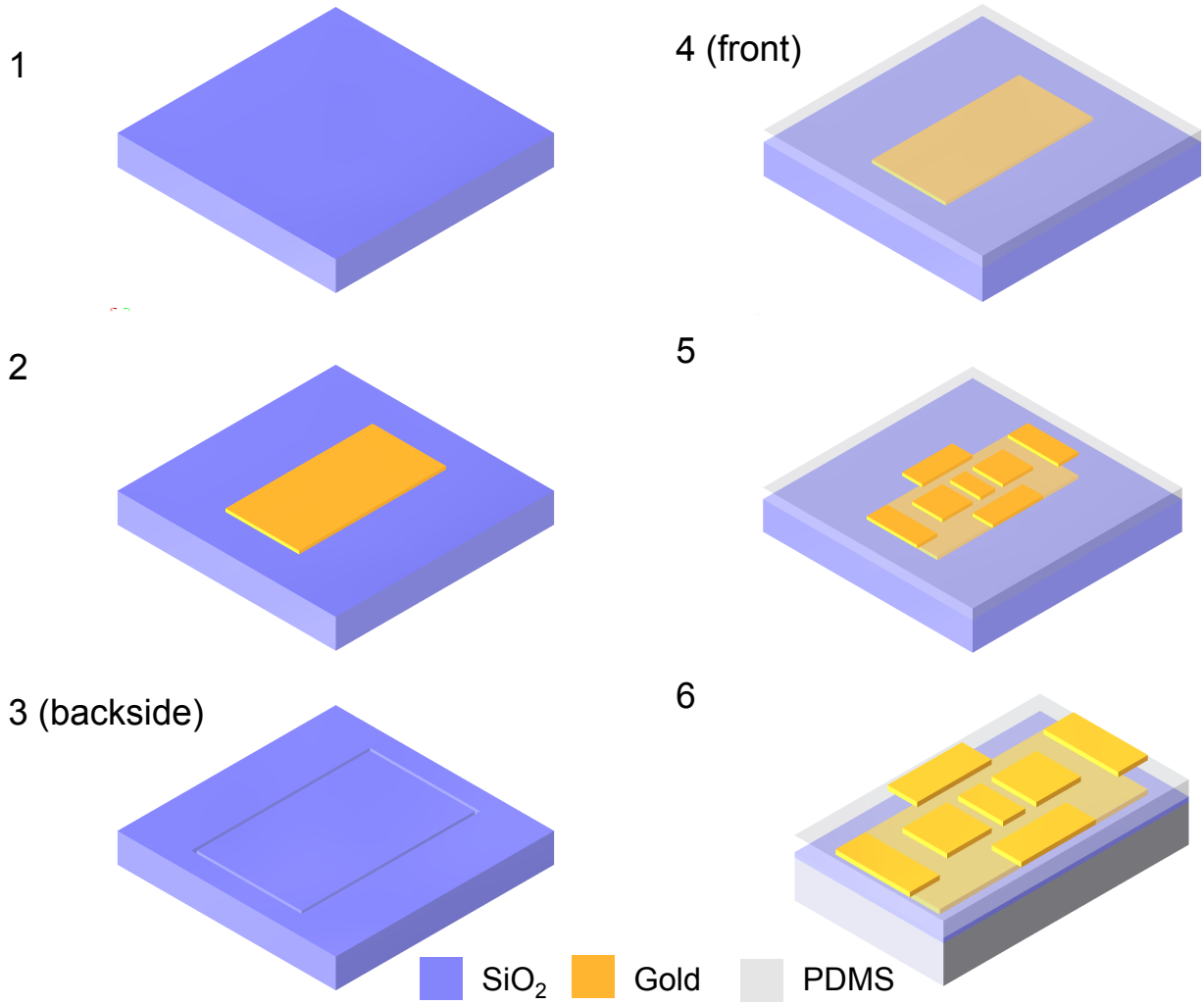

Figure 20. Sensor fabrication steps of the combined compression and shear sensor. (1) The fabrication began with an oxidized substrate to isolate the single. (2) The bottom metal plate was photolithographically defined and realized by liftoff of an evaporated titanium and gold layer. (3) Cleaving lines were etched into the backside of the wafer to simplify isolation of the individual sensors after fabrication was completed. (4) The wafers were then spin-coated with a thin polydimethylsiloxane (PDMS) layer to separate the top and bottom metal plates. (5) The top metal elements were also photolithographically defined and lifted off to reveal the final gold electrodes. (6) The samples were cleaved and isolated for testing and ultimately for integration with the grasper.

Similar short-loop experiments were conducted for metal evaporation on PDMS. These experiments helped address cracking and delamination issues associated with the temperature and pressure of evaporated metal. After success with the short-loop experiments, the top electrode was evaporated and patterned to reveal the final sensor. The wafers were each partially anisotropically etched from the backside with a deep reactive ion-etching (DRIE) tool to create cleaving lanes to help singulate the devices.

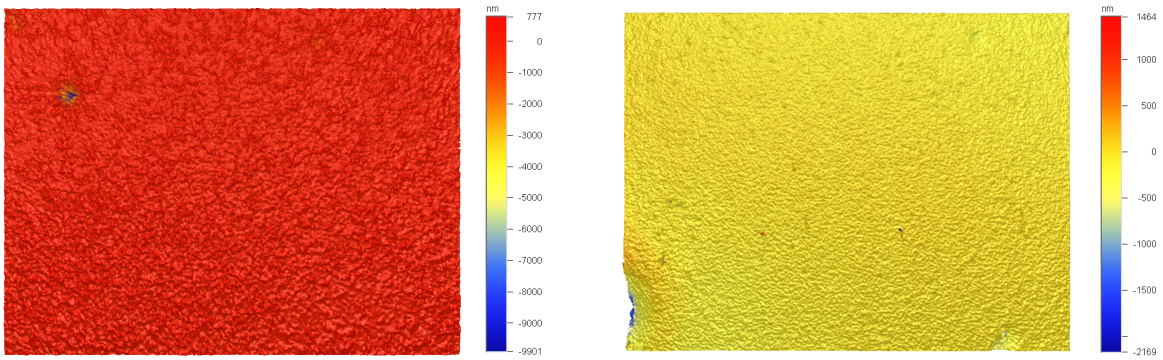

Figure 21. Interferometer measurement of metal on PDMS. (left) The profile shows the metal was successfully deposited on the PDMS surface without cracking and the average surface roughness is ~1 micron. (right) The profile shows the bare PDMS surface with average surface roughness of ~0.5 micron as a comparison.

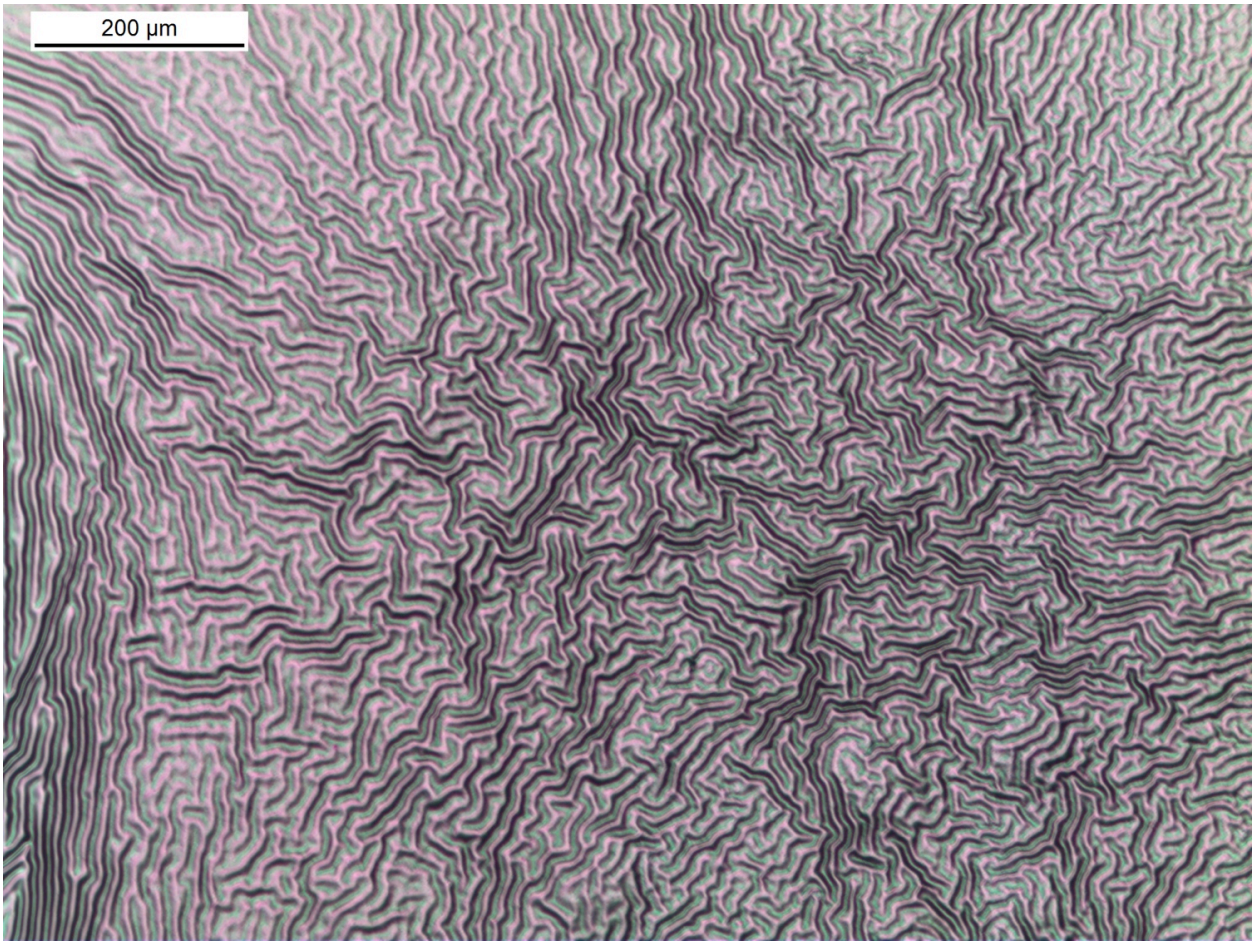

Figure 22. Ridges and grooves of PDMS substrate with a thin evaporated metal blanket.

Evaporation of metal on PDMS resulted in apparent ridges and grooves on the surface. This created a surface roughness on the order of 1 micron. While this does affect the appearance of the sensor elements, it does not affect device performance and results in a slight change in the baseline capacitance of 3% (1 micron on a 35 micron dielectric). Interferometer measurements show the metal surface, while grooved, does not contain any cracks which would result in separate capacitive elements and issues with backend processing like soldering and integration with the circuit. As a comparison, the roughness of the metal on PDMS was compared to the roughness of the bare PDMS surface, which is twice as smooth.

3.2 Printed Circuit Board (PCB) Fabrication

Although wafer level testing does not require a read out circuit, application as an intra-operative sensor does require a small-footprint circuit board. Printed circuit boards for both the parallel plate and the combined sensor were developed.

3.2.1 **Parallel Plate PCB**

A switching circuit was designed in the group to characterize the singulated sensor response to an applied load. The switches (Figure 23) are shorted when the input is high and open otherwise. Because of the Schmitt trigger inverter, the condition where switch one is on and switch two is off is represented in Figure 24 (left) and the opposite condition creates the output in Figure 24 (right). This switching, between both conditions defines how the circuit oscillates.

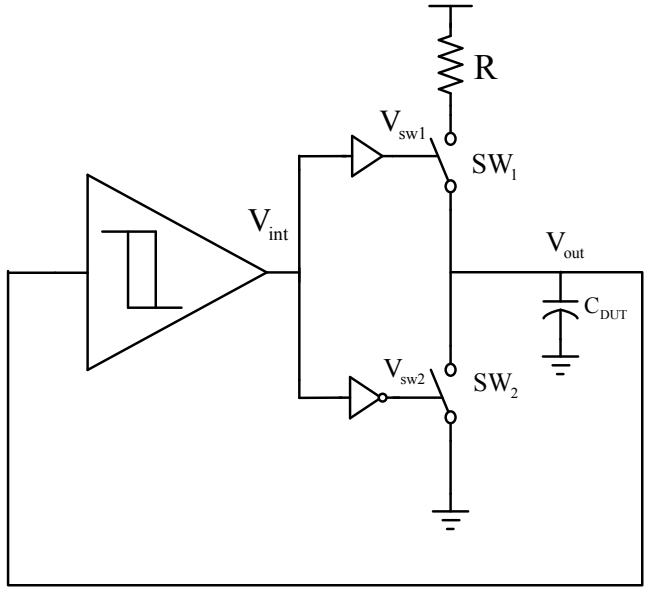

Figure 23. Schematic of the capacitive sensing circuit. The circuit is composed of a Schmitt trigger buffer, inverter, buffer, two switches, resistor and the sensing capacitor (C_{DUT}).

Precise measurement of the frequency output of the circuit could be used to determine the capacitance. Yet, parasitics can distort the signal significantly resulting in misinterpretation of the capacitance and therefore the applied load. Additionally, practical application of this circuit would require a large table-top frequency counter, which would impact mobility and use in the operating room. Finally, a differential measurement, where the unloaded condition results in an output of 0 Farads, would cause an unstable frequency response from the circuit. For those reasons, a new approach was required for a combined compressive and shear sensor.

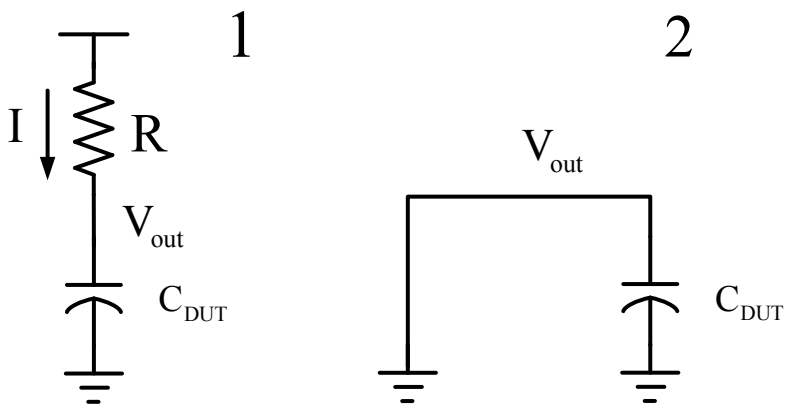

Figure 24. Equivalent circuits for phase 1 and phase 2.

3.2.2 **Combined Sensor PCB**

The combined sensor was integrated with a custom circuit board designed with Altium Designer layout software and manufactured by FlexPCB. The board consisted of footprints for two separate Agilent AD7746 capacitance to digital converter chips (CDC), one for compression and one for shear sensing, and the passive components required for proper operation of the CDCs.

The chips were chosen for their high resolution and fast sampling rate, which are both crucial for the capacitors designed, as well as the latency requirements for a tactile feedback system.

The resolution of the sensor system is a direct result of the noise performance of the circuit and, ultimately, the resolution is the noise divided by the sensitivity. The sensitivity is a function of the physical sensor parameters. The measured noise was on the order of 100s of attoFarads and therefore, we are able to achieve sub-Newton resolution with the current sensor and circuit.

The resolution can be improved with improved shielding, to reduce noise, and this will be a focus of the next generation sensor/circuit system being developed.

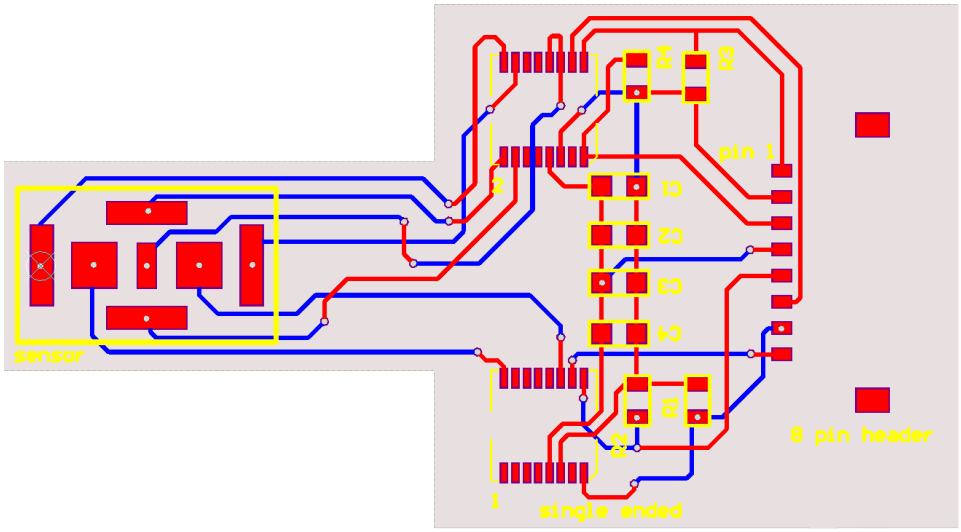

Figure 25. Schematic of printed circuit board design layout. The 2 layer board allowed for multiple connections to the 7-electrode configuration of the combined compression and shear sensor. The board was designed to integrate with the analog sensor output on one end and digitized by separate capacitance to digital chips for shear and compression sensing.

Figure 26, shows the circuit layout. Importantly, a second modification that is also being implemented on a second revision of the circuit is a much longer board layout.

The overall length of the first generation board is 3 inches. For surgical applications, the sensor must be at the grasper tip, while the rest of the electronics should be outside the body. This will help reduce sterilization complications, and will minimize the risk of unforeseen issues of electronics in a liquid-filled and tight cavity—the human body.

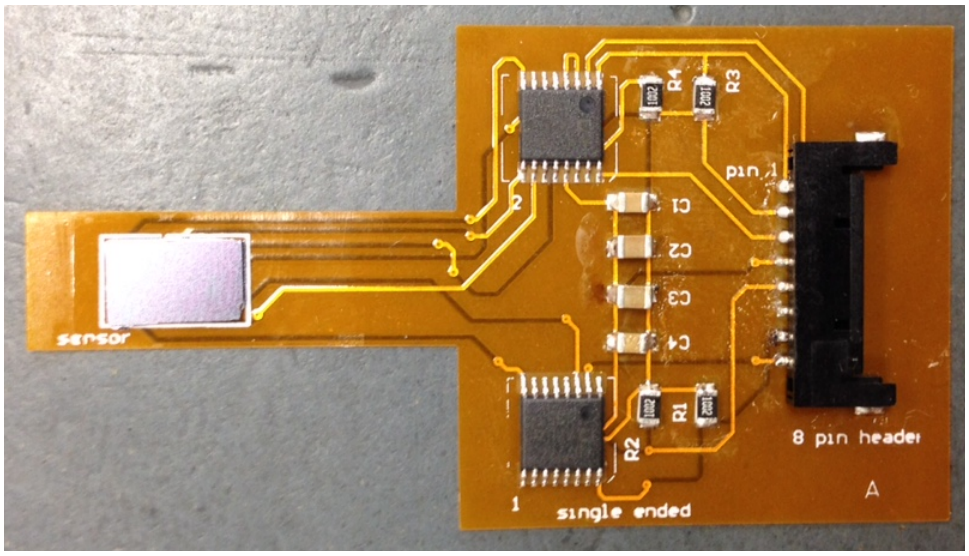

Figure 26. Populated printed circuit board. The final sensor was integrated with the board with the backside of the substrate exposed. This allowed for the protection of the delicate front side of the sensor, distribution of the load over the entire sensor surface, and simple one-sided integration with the PCB.

Chapter 4 **Results**

4.1 Parallel Plate Capacitor

In the field, each sensor would require a read out circuit. However, wafer level benchtop testing for characterization of the sensor performance does not require a read-out circuit as the probes of an impedance analyzer directly connect to the sensor bond pads in a 4-point configuration which is ideal for sensing low impedances and therefore sensitive measurements. The test setup can be used to measure a number of different parameters including impedance and capacitance as a function over a broad frequency spectrum. The impedance analyzer was used in this work to determine the baseline capacitance of the fabricated sensors as a validation of the fabrication process and comparison to the calculated capacitance.

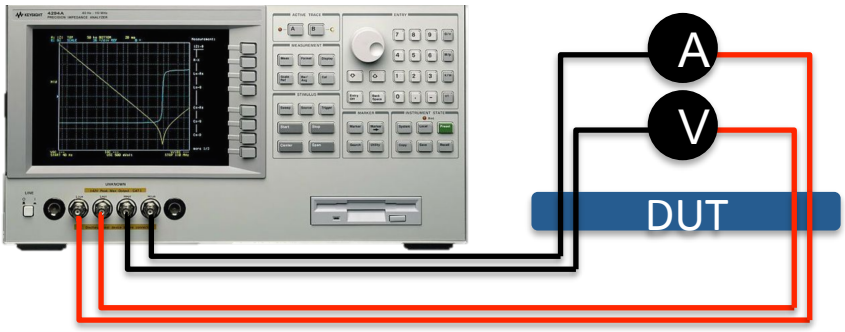

Figure 27. Schematic illustration of testing setup for wafer-level sensor characterization. An Agilent 4294A precision impedance analyzer in a four-point testing configuration is used to simultaneous stimulate and measure the performance of the capacitive sensor over a range of frequencies.

The results of the baseline testing are plotted in Figure 28. The central trace represents the mean measurement of six sensor elements with the standard deviation plotted as a dashed envelope around the mean. The measured capacitance agrees well with the theoretical capacitance to within 3% and the frequency dependence is due to

the frequency dependent permittivity of the Parylene-C. This data represents the unloaded sensor, while Figure 30 depicts the sensor output in response to various load conditions.

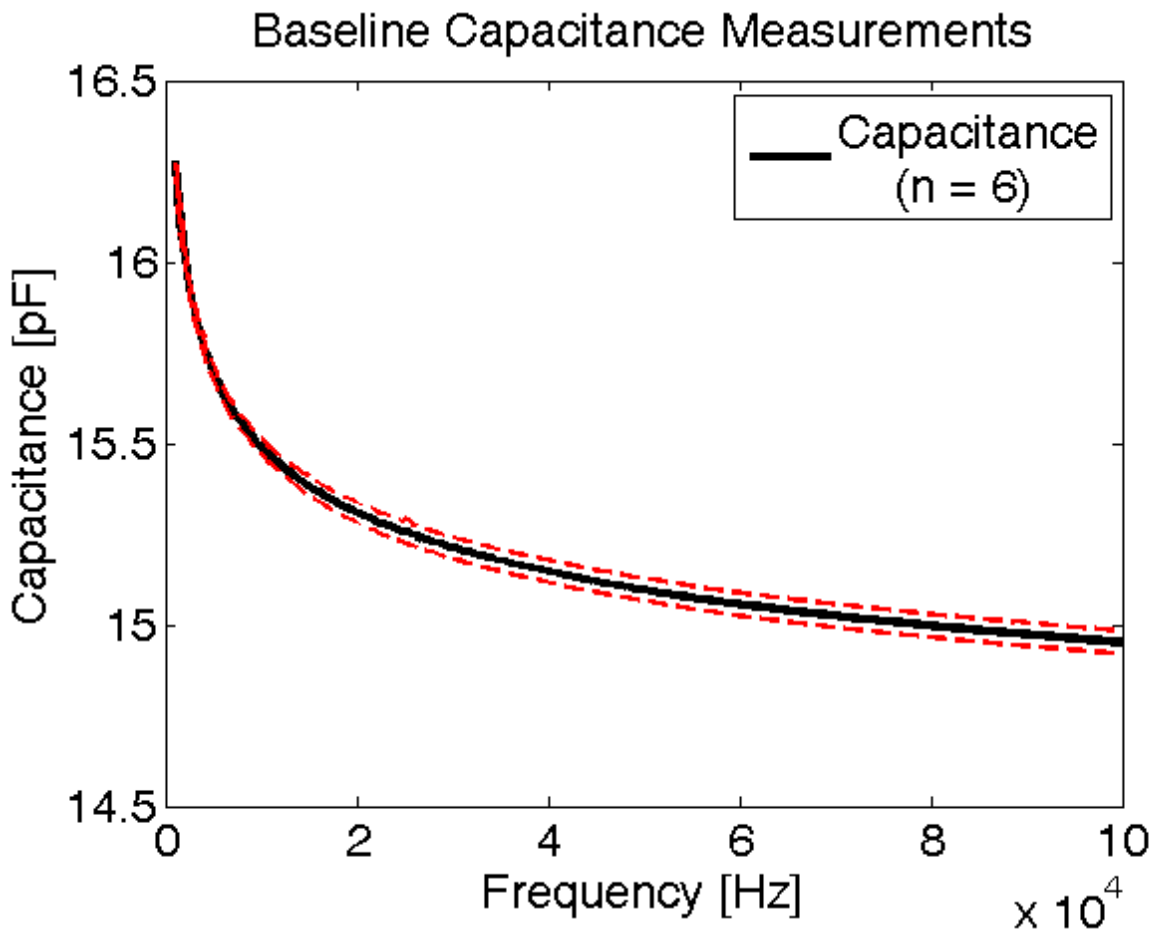

Figure 28. Measured baseline capacitance. The mean and standard deviation (dashed lines) of six capacitive sensors from a single capacitive array are plotted as a function of the measurement frequency. The frequency-dependent behavior of the sensor is due to the non-constant dielectric constant of the Parylene C dielectric material. The measured capacitance exhibits a 2.5% error from theoretically predicted values.

The sensor must respond to applied loads, and this response is modulated and determined by the dielectric material. Materials with a low elastic modulus would result in high sensitivity but low dynamic range as the sensor will quickly saturate at low loads.

Dielectric materials with larger elastic modulus will result in the ability to sense over a large dynamic range, but with relatively low sensitivity. Therefore, material selection that gives both the appropriate sensitivity and dynamic range is crucial. Parylene C is one material that responds well over typical surgical loads. The data points represent the capacitive output in picoFarads in response to an applied load. A linear trendline is also overlaid on the data. The sensitivity of the sensor output, agrees well with the theoretical sensitivity calculations to within 2%. Additionally, the sensor responds linearly over a minimum of a 10-N range (testing was not done at larger loads). This testing was completed at the wafer level with the impedance analyzer and load cell for quantification (Figure 29).

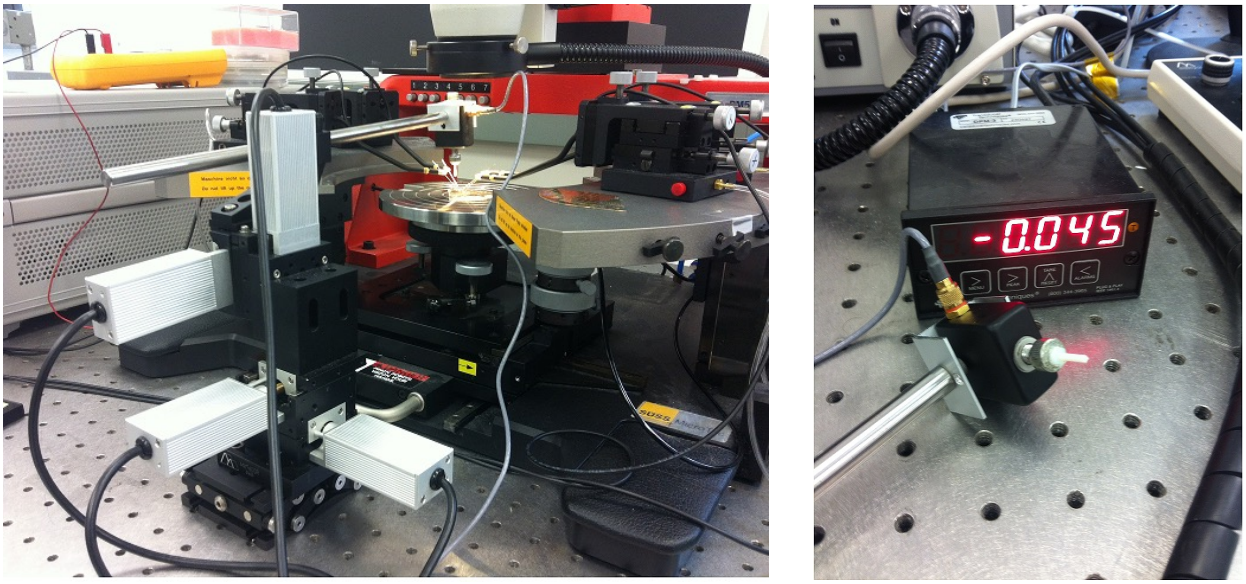

Figure 29. Wafer-level compression testing setup. (Left) A 4-axis micromanipulator applies a vertical load to the capacitive sensor. The capacitance is measured through the probes and the adjacent impedance analyzer. (right) A close up of the force applicator and the load cell.

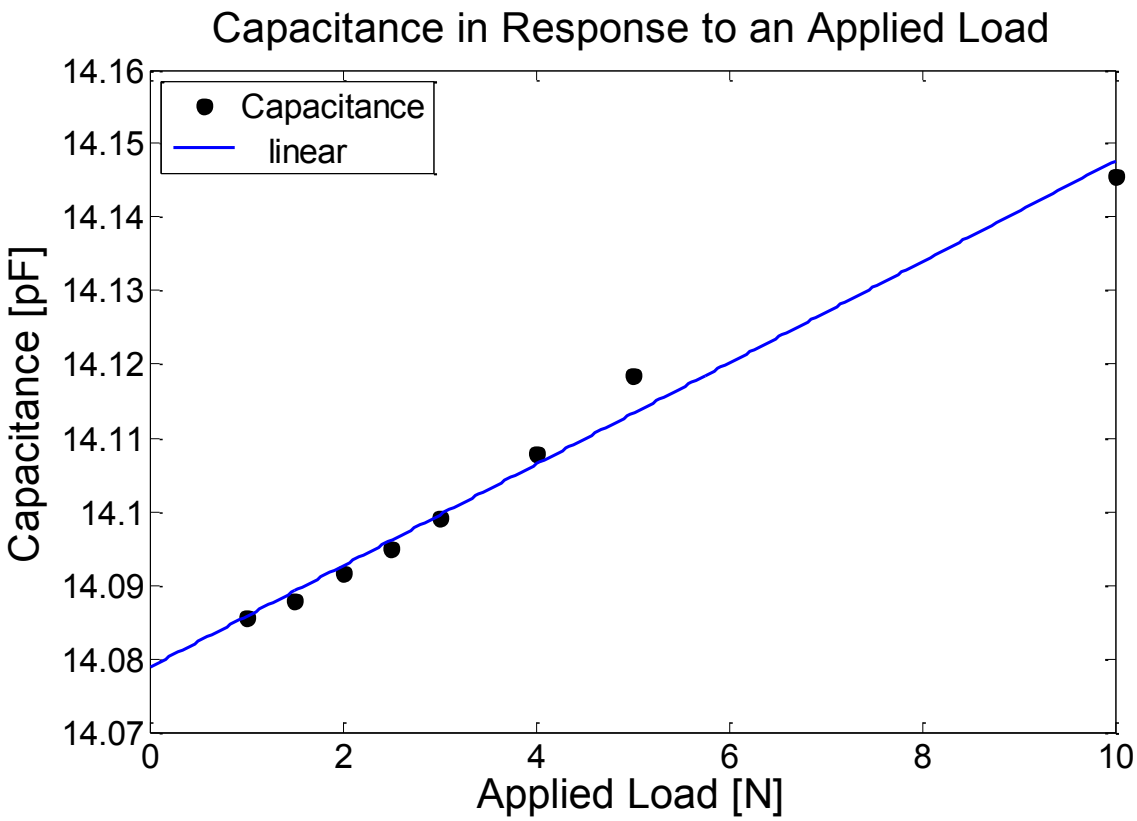

Figure 30. Capacitive response to an applied load. The sensor was subjected to progressive loads and the output capacitance was plotted for each applied load. A solid line represents the linear fit of the response, the slope of which corroborates with the calculated capacitive sensitivity. The expectation is that compressive loads decrease the size of the gap between the top and bottom plate, resulting in an increase in the capacitance.

Because the sensors are to be ultimately deployed in the surgical field, it would be impractical to require an impedance analyzer in the operating room. Therefore, the wafers were diced to reveal individual sensor arrays, which could be wire bonded to a custom-built switching circuit developed in the laboratory. The frequency of the output of the circuit was dictated by a 1/RC time constant and a saw tooth voltage trace. The unloaded sensor would therefore output at a specific, constant frequency, and application of a compressive load would create a perturbation from this baseline value.

By reasoning, this perturbation would always create a decrease in the frequency of the output. More explicitly, a compressive load would reduce the size of the gap between the two parallel plates of the capacitor and would result in an increase in the capacitance. Because the capacitance is in the denominator of the time constant equation, this would result in a downward shift in frequency.

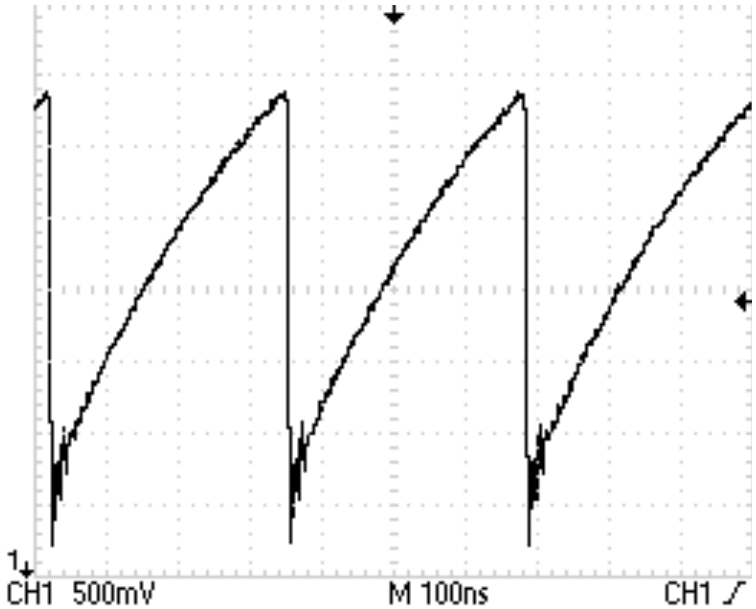

Figure 31. Output of a Schmitt trigger switching circuit. The frequency of the output is inversely proportional to the capacitance and more specifically to the inverse of the time constant. Essentially, as the capacitance increases the frequency of the switching circuit decreases.

The output of the Schmitt trigger circuit was fed into a frequency counter and binned according to frequency. The baseline (unload) sensor created a switching frequency of 3.02 MHz. When a 1 Newton load was applied to the top plate of the sensor, the output frequency decreased by 2 kHz to 3.018 MHz. This small, but significant change created by the load could be used to determine applied loads during surgical applications.

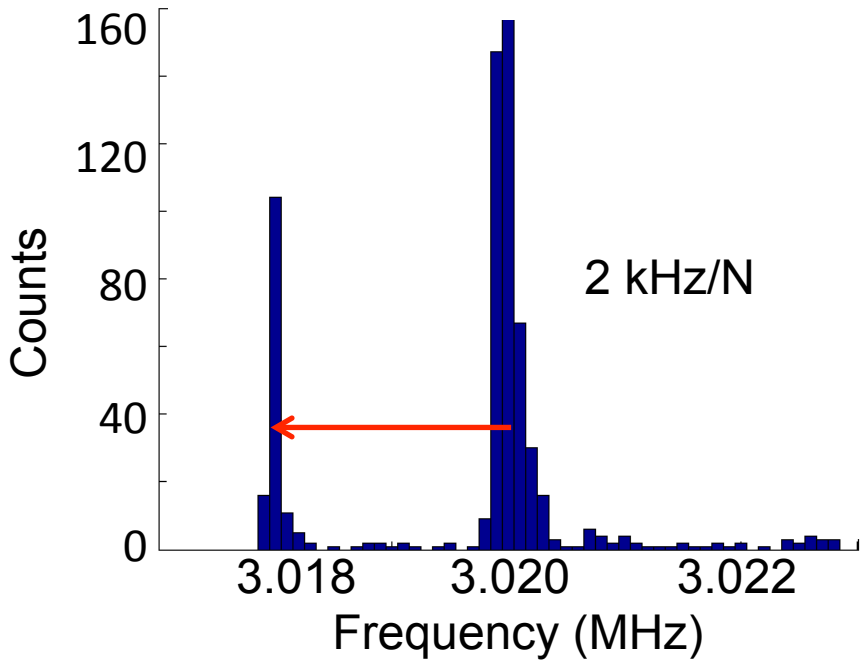

Figure 32. Histogram of the number of counts of frequency from the output of the switching circuit. The switching circuit was fed into a frequency counter where the baseline frequency was 3.02 MHz. A one-newton load was applied to the capacitive sensor and the frequency of the circuit shifted downward. The response was measured to be 2 kHz/N.

4.2 Combined Compressive and Shear Sensor

The circuit was able to output both a single ended measurement for the compression sensing and shear sensing in both the lateral and transverse direction. The sensor was then subjected to calibrated compressive loads to characterize the output and provide a basis for comparison to the theoretical values of the sensor in response to an applied load as well as validation of the sensor fabrication.

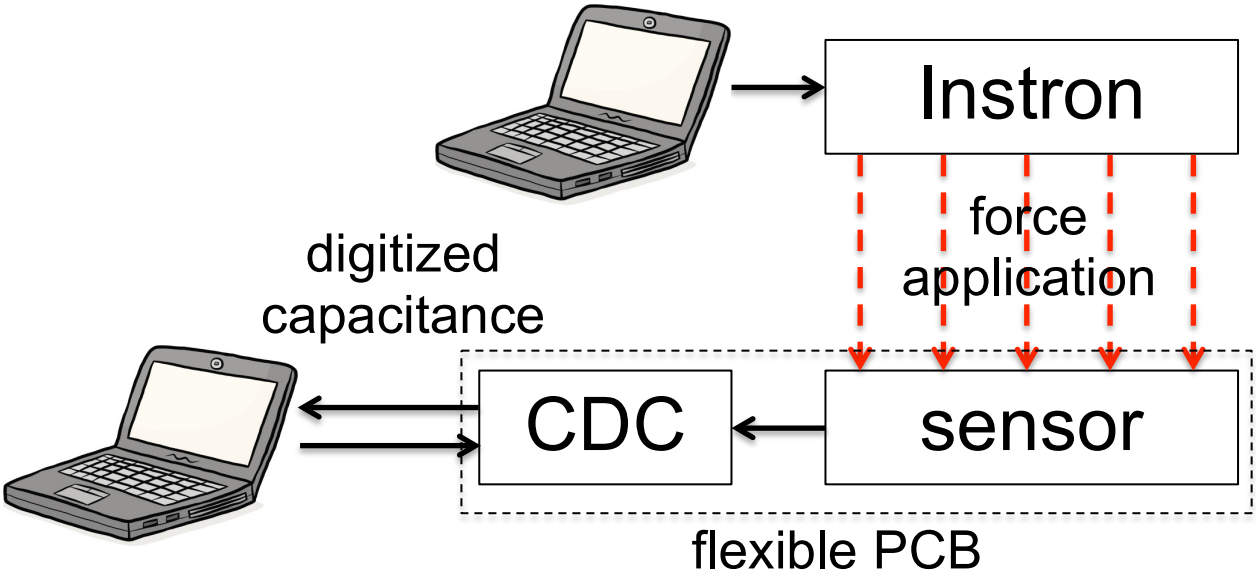

Figure 33. The test setup for compression sensing. Forces were applied by an Instron universal testing machine onto the sensor surface. The capacitance to digital chip gave a direct digital output from the sensor, which was captured by the sensor software. The same PC powered the capacitance to digital converter chip (CDC), while a separate PC controlled the application of force.

A personal computer (PC) controls an Instron universal testing machine to apply quantized loads onto the sensor surface. This load creates a change in the capacitance, which is captured by a separate PC where the data is analyzed. The data is presented in Figure 34. Here the normalized capacitance data is plotted against the applied load, where the maximum load the sensor was subjected to was 30 N. The data is plotted along side the theoretical calculation for a sensor with the same dimensions as the one fabricated. Generally, the data agrees with the calculation. The force application system, is not the ideal application system because an Instron is not designed to hold at a particular load, but instead, to actuate a prescribed strain rate and output the compressive or tensile stress. Therefore, because of this drift, the capacitive data is not in perfect agreement with the theoretical line. However, this first data *does* support the

use of our capacitive sensors for robotic surgical systems. The error bars represent the standard deviation of the data, n = 3. Yet, simple parallel plate capacitors have already been presented in this work, so on it's own, this is result is relatively marginal. Combined with a responsive shear component, the sensor would be valuable to surgeons for reducing grip force and preventing adverse effects during surgery.

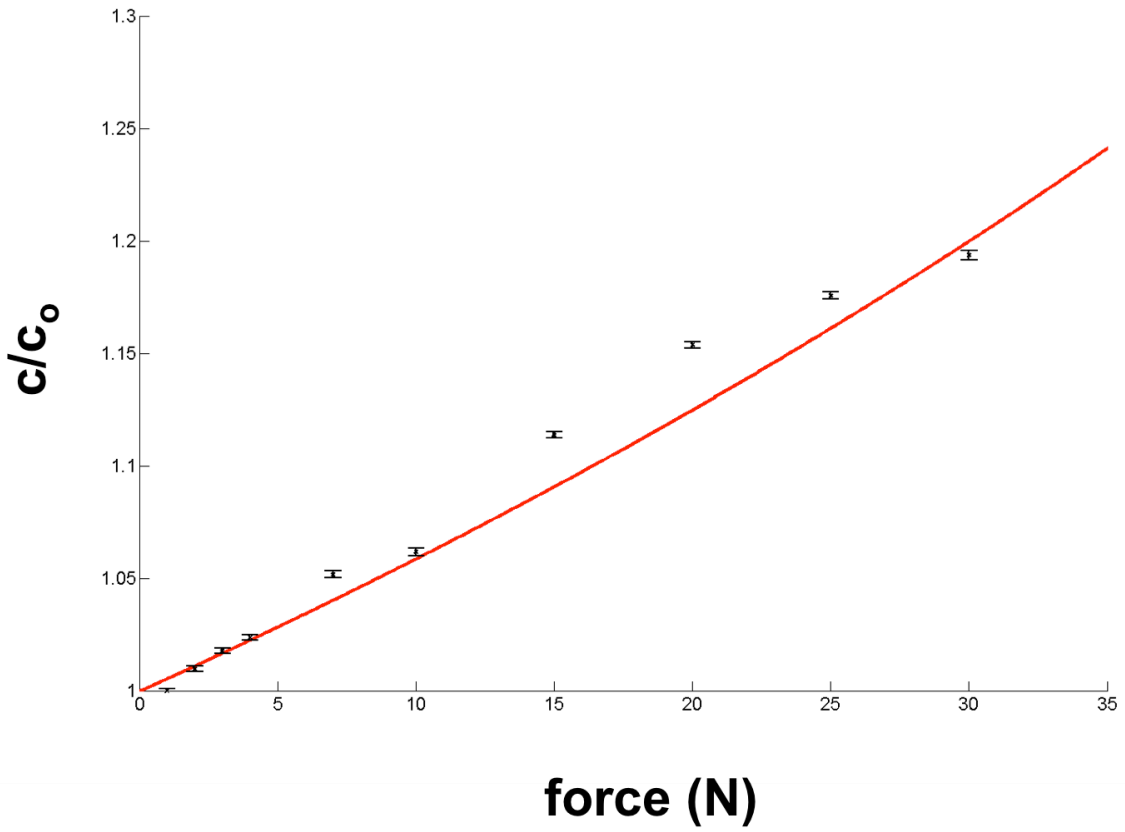

Figure 34. The sensor output in response to a compressive load. The theoretical sensor output, in terms of relative change to the baseline value, is presented by a red trace. The data points are the measured output as a function of the applied load in Newtons.

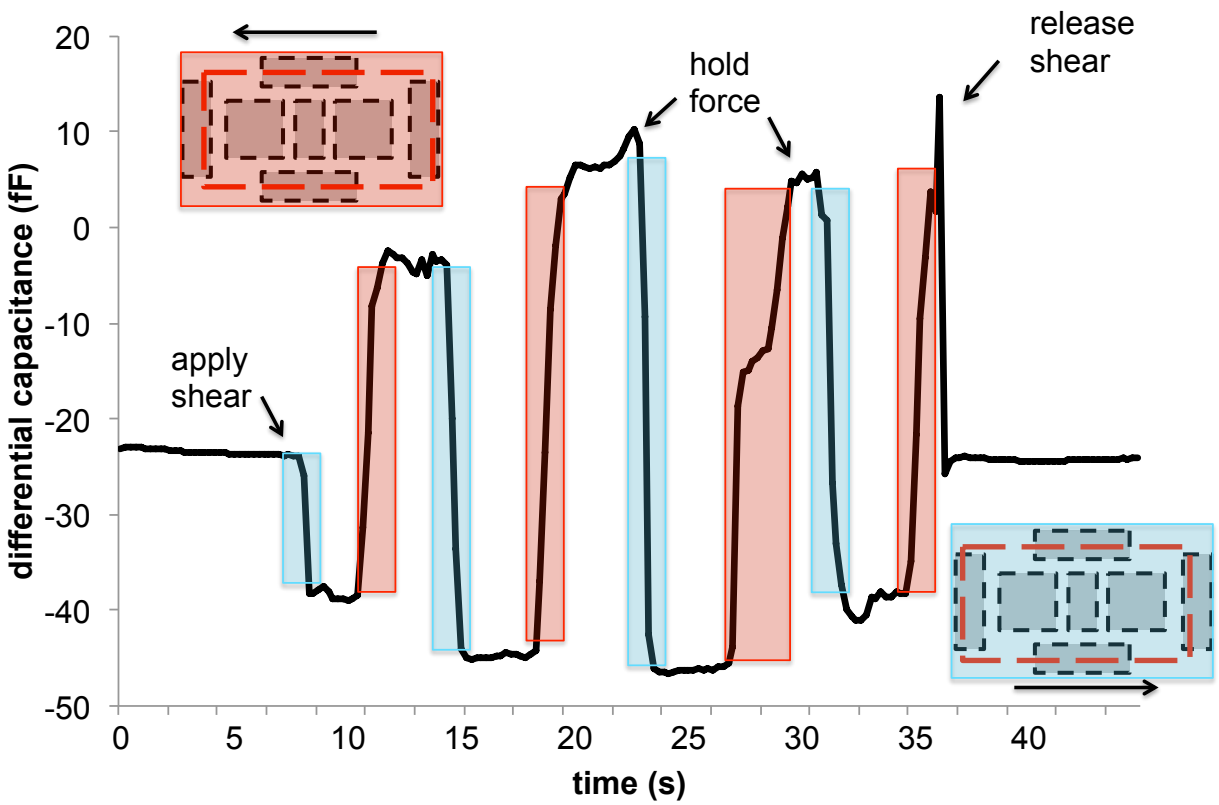

Figure 35. The shear response of the combined sensor. The blue and pink semi-transparent bars on the plot represent shear in the positive and negative x direction, respectively. Shear in the positive x direction resulted in a negative differential capacitance, while shear in the negative x direction resulted in a positive differential measurement. Positive and negative peaks represent a static load condition in either direction. Release of the applied load resulted in a return to baseline. The initial offset from zero resulted from alignment error during the fabrication process where the area of the sensor elements over the bottom electrode plate was not identical.

Figure 35 shows the output of the shear-sensing portion of the sensor. Here the sensor is sheared along the axial dimension (x-direction in Figure 14). Light blue bars represent pulling in the +x direction and pink bars represent a shear in the –x direction. Qualitatively, the sensor responds to shear in both directions and is proportional to the magnitude of the shear. Prior to the application of the shear, there is a non-zero offset,

which can be defined by equation 19 (Section 2.4.2.2), the nonzero baseline differential capacitance corresponds with roughly a 25 micron misalignment.

$$C_x = \frac{\varepsilon}{2z}\left(\frac{s^2 ly}{s^2 - 4y^2}\right) \tag{25}$$

As a reminder, because this is a differential output, the assumption is that without a shear load, the output of both sensors should be identical and therefore the differential should be zero. However, with misalignment during the fabrication, the baseline overlap was not identical and therefore, a non-zero differential capacitance prior to application of a shear load. Release of the load returns to this original non-zero baseline.

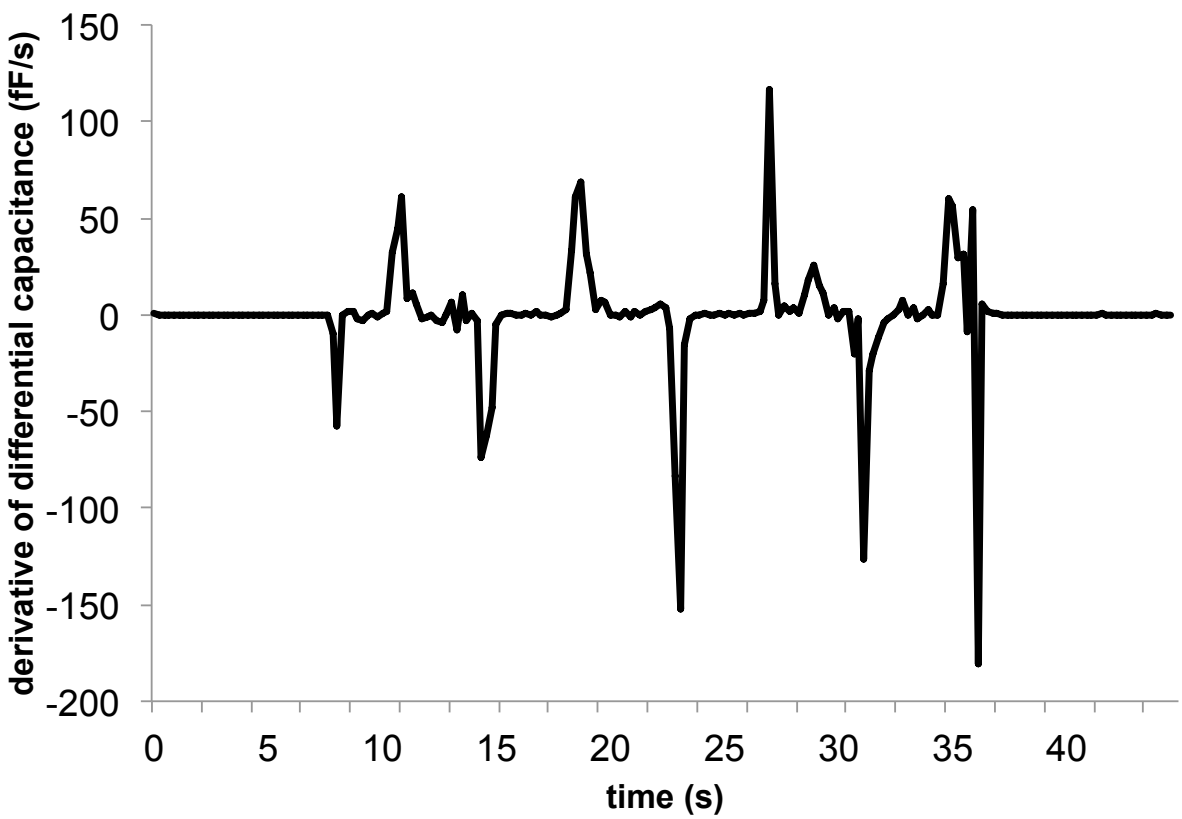

Figure 36. Derivative of the shear sensor output from the data in figure 34. Real-time calculations of the derivative of the shear plot could give indications of slipping events.

Interestingly, the acquisition of shear data can also be used to impose virtual walls or improved gripping, assuming algorithms can be developed with minimal latency. The derivative, or the rate of change, of the shear sensor output can be used to detect slipping events. In combination with the compressive load data, if a sharp peak is seen in the rate of change of the shear sensor, one could postulate that slip has occurred and autonomously apply increased grip force to grasp the tissue and avoid slipping. This same algorithm could be applied to suturing tasks or other surgical tasks, where slip could be problematic. In addition, shear data could be used to impose virtual walls to prevent excessive tension on sutures. If the material and gauge of the suture could be input into the surgical system, the robot could limit the tensile stress applied on sutures, such that premature rupturing does not occur during knotting.

4.3 Summary and Conclusion

Capacitive sensors have been designed and fabricated to be integrated onto the grasping area of minimally invasive surgical tools. Integration of sensors, and later arrays, will give the surgeon a picture of the interactions at the tissue interface. This will help avoid intraoperative issues including tissue crush injuries and suturing challenges. The work here identified several sensing modalities and compared the properties of each for surgical applications. After consideration, capacitive sensors were chosen due to their small footprint, time response, and simplicity. A first generation sensor was design for simple compressive load detection and quantification for use during surgery. These sensors could not detect tangential loads, which are common during suturing and

palpation tasks. A combined shear and normal capacitive sensor was designed to accommodate those deficiencies with a separate shear sensing component. The combined compressive and shear sensor could be integrate with grasper to detect all aspects of surgical tasks to prevent tissue crush injuries and suture rupturing. Future work to quantify the shear sensor performance, integrate with a robotic surgical platform are underway. This will serve to improve patient care, while enhancing the surgeon's ability to perform more complicated procedures. Real time load information can also be used to impose virtual walls, which can prevent the application of excessive loads and could also be used to transition to completely autonomous surgical procedures, where optimized loads can be applied to tissues and robotic surgical can detect slip events and augment loads to prevent slip or other potential surgical accidents.

REFERENCES

[1] C. Tsui, R. Klein, and M. Garabrant, "Minimally invasive surgery: national trends in adoption and future directions for hospital strategy," *Surgical Endoscopy and Other Interventional Techniques,* vol. 27, pp. 2253-2257, Jul 2013.

[2] H. v. Jacobaeus, "Über die Möglichkeit die Zystoskopie bei Untersuchung seröser Höhlungen anzuwenden," *Münch Med Wochenschr,* vol. 57, pp. 2090-2092, 1910.

[3] M. Hatzinger, S. T. Kwon, S. Langbein, S. Kamp, A. Hacker, and P. Alken, "Hans Christian Jacobaeus: Inventor of Human Laparoscopy and Thoracoscopy," *Endourology,* vol. 20, pp. 848-850, 2006.

[4] H. de Kok, "A new technique for resecting the non-inflamed not-adhesive appendix through a mini-laparotomy with the aid of the laparoscope," *Archivum chirurgicum Neerlandicum,* vol. 29, p. 195, 1977.

[5] J. Tarasconi, "Endoscopic salpingectomy," *Journal of Reproductive Medicine,* vol. 26, pp. 541-5, 1981.

[6] G. S. Litynski, "Kurt Semm and the Fight against Skepticism: Endoscopic Hemostasis, Laparaoscopic Appendectomy, and Semm's Impact on the "Laparoscopic Revolution"," *JSLS,* vol. 2, pp. 309-313, 1998.

[7] K. Semm, "Endoscopic appendectomy," *Endoscopy,* vol. 15, pp. 59-64, 1983.

[8] C. A. Blum and D. B. Adams, "Who did the first laparoscopic cholecystectomy?," *J Minim Access Surg,* vol. 7, pp. 165-8, Jul 2011.

[9] N. C. f. H. Statistics, "National Hospital Discharge Survey: 2010 Table," 2010.

[10] C. Tsui, R. Klein, and M. Garabrant, "Minimally invasive surgery: national trends in adoption and future directions for hospital strategy," *Surg Endosc,* vol. 27, pp. 2253-7, Jul 2013.

[11] N. Transparency Market Research of Albany, "Minimally Invasive Surgery Market (Surgical Devices, Monitoring & Visualization Devices, and Endoscopy Devices) - Global Industry Analysis, Size, Share, Growth, Trends and Forecast, 2013 through 2019," 2013.

[12] "Number of all-listed procedure for discharge from short-stay hospitals, by procedure category and age: United States, 2010," *CDC/NCHS National Hospital Discharge Survery,* 2010.

[13] M. A. Cooper, Ibrahim, A., Lyu, H. and Makary, M. A. , "Underreporting of Robotic Surgery Complications," *Journal for Healthcare Quality,* 2013.

[14] M. Kitagawa, A. M. Okamura, B. T. Bethea, V. L. Gott, and W. A. Baumgartner, "Analysis of Suture Manipulation Forces for Teleoperation with Force Feedback," in *Medical Image Computing and Computer-Assisted Intervention — MICCAI 2002: 5th International Conference Tokyo, Japan, September 25–28, 2002 Proceedings, Part I*, T. Dohi and R. Kikinis, Eds., ed Berlin, Heidelberg: Springer Berlin Heidelberg, 2002, pp. 155-162.

[15] Y. S. Kwoh, J. Hou, E. A. Jonckheere, and S. Hayati, "A robot with improved absolute positioning accuracy for CT guided stereotactic brain surgery," *Biomedical Engineering, IEEE Transactions on,* vol. 35, pp. 153-160, 1988.

[16] A. R. Lanfranco, A. E. Castellanos, J. P. Desai, and W. C. Meyers, "Robotic surgery - A current perspective," *Annals of Surgery,* vol. 239, pp. 14-21, Jan 2004.

[17] S. De, J. Rosen, A. Dagan, B. Hannaford, P. Swanson, and M. Sinanan, "Assessment of tissue damage due to mechanical stresses," *International Journal of Robotics Research,* vol. 26, pp. 1159-1171, Nov 2007.

[18] C. J. Mohr, G. S. Nadzam, and M. J. Curet, "Totally robotic Roux-en-Y gastric bypass," *Archives of Surgery,* vol. 140, pp. 779-785, Aug 2005.

[19] C. R. Wagner, Stylopoulos, Nicholas, Jackson, Patrick G., Howe, Robert D., , "The Benefit of Force Feedback in Surgery: Examination of Blunt Dissection," *Teleoperators and Virtual Environments,* vol. 16, pp. 252-262, 2007.

[20] M. Z. Stephens TK, Sweet RM, Kowalewski TM., "Tissue Identification Through Back End Sensing on da Vinci EndoWrist Surgical Tool," *ASME. J. Med. Devices,* vol. 9, 2015.

[21] A. Sie, Winek, M., and Kowalewski, T.M., "Online Identification of Abdominal Tissues In Vivo for Tissue-Aware and Injury-Avoiding Surgical Robots," *Intelligent Robots and Systems (IROS),* September 14-18, 2014 2014.

[22] D.-H. Lee, Kim, U, Gulrez, T, Yoon, WJ, Hannaford, B and Choi, HR, "A Laparoscopic Grasping Tool with Force Sensing Capability," *IEEE/ASME Transactions on Mechatronics,* 2015.

[23] R. Ahmadi, Arbatani, S., Packirisamy, M., Dargahi, J, "Micro-optical force distribution sensing suitable for lump/artery detection," *Biomed Microdevices,* vol. 17, 2015.

[24] U. Kim, Lee, D.H., Moon, H., Koo, J.C., and Choi, H.R., "Design and Realization of Grasper-Integrated Force Sensor for Minimally Invasive Robotic Surgery," *2014 IEEE/RSJ Internation Conference on Intelligent Robots and Systems (IROS 2014),* September 14-18 2014.

[25] U. Kim, Lee, D.H., Yoon, J., Hannaford, B., and Choi, H.R., "Force Sensor Integrated Surgical Forceps for Minimally Invasive Robotic Surgery," *IEEE Transactions on Robotics,* vol. 31, pp. 1214-1224, 2015.

[26] P. Puangmali, et al., "State-of-the-art in force and tactile sensing for minimally invasive surgery," *Sensors Journal,* vol. IEEE 8.4, pp. 371-381, 2008.

[27] J. Marescaux, Leroy, J., Gagner, M., Rubino, F., Mutter, D., Vix, M., Butner, S.E., Smith, M.K., "Transatlantic robot-assisted telesurgery," *Nature,* vol. 413, pp. 379-380, 2001.